arXiv:1105.3470v1 [astro-ph.CO] 17 May 2011

THE *HUBBLE SPACE TELESCOPE* CLUSTER SUPERNOVA SURVEY: V. IMPROVING THE DARK ENERGY CONSTRAINTS ABOVE $Z > 1$ AND BUILDING AN EARLY-TYPE-HOSTED SUPERNOVA SAMPLE *

N. SUZUKI[1,2], D. RUBIN[1,2], C. LIDMAN[3], G. ALDERING[1], R. AMANULLAH[2,4], K. BARBARY[1,2], L. F. BARRIENTOS[5], J. BOTYANSZKI[2], M. BRODWIN[6,7], N. CONNOLLY[8], K. S. DAWSON[9], A. DEY[10], M. DOI[11], M. DONAHUE[12], S. DEUSTUA[13], P. EISENHARDT[14], E. ELLINGSON[15], L. FACCIOLI[1,2], V. FADEYEV[16], H. K. FAKHOURI[1,2], A. S. FRUCHTER[13], D. G. GILBANK[17], M. D. GLADDERS[18], G. GOLDHABER[44], A. H. GONZALEZ[19], A. GOOBAR[4,20], A. GUDE[2,21], T. HATTORI[22], H. HOEKSTRA[23], E. HSIAO[1,2], X. HUANG[1,2], Y. IHARA[11,25], M. J. JEE[26], D. JOHNSTON[12,27], N. KASHIKAWA[28], B. KOESTER[18,29], K. KONISHI[30], M. KOWALSKI[31], E. V. LINDER[1,2], L. LUBIN[26], J. MELBOURNE[36], J. MEYERS[1,2], T. MOROKUMA[11,25,28], F. MUNSHI[2,32], C. MULLIS[33], T. ODA[34], N. PANAGIA[13], S. PERLMUTTER[1,2] M. POSTMAN[13], T. PRITCHARD[2,35], J. RHODES[14,36], P. RIPOCHE[1,2], P. ROSATI[37], D. J. SCHLEGEL[1], A. SPADAFORA[1], S. A. STANFORD[26,38], V. STANISHEV[20,39], D. STERN[14], M. STROVINK[1,2], N. TAKANASHI[28], K. TOKITA[11], M. WAGNER[40], L. WANG[41], N. YASUDA[42], H. K. C. YEE[43],
(THE SUPERNOVA COSMOLOGY PROJECT)
Draft version May 18, 2011

Abstract

We present ACS, NICMOS, and Keck AO-assisted photometry of 20 Type Ia supernovae (SNe Ia) from the HST Cluster Supernova Survey. The SNe Ia were discovered over the redshift interval $0.623 < z < 1.415$. Fourteen of these SNe Ia pass our strict selection cuts and are used in combination with the world's sample of SNe Ia to derive the best current constraints on dark energy. Ten of our new SNe Ia are beyond redshift $z = 1$, thereby nearly doubling the statistical weight of HST-discovered SNe Ia beyond this redshift. Our detailed analysis corrects for the recently identified correlation between SN Ia luminosity and host galaxy mass and corrects the NICMOS zeropoint at the count rates appropriate for very distant SNe Ia. Adding these supernovae improves the best combined constraint on dark energy density, $\rho_{\rm DE}(z)$, at redshifts $1.0 < z < 1.6$ by 18% (including systematic errors). For a flat ΛCDM universe, we find $\Omega_\Lambda = 0.729^{+0.014}_{-0.014}$ (68% CL including systematic errors). For a flat wCDM model, we measure a constant dark energy equation-of-state parameter $w = -1.013^{+0.068}_{-0.073}$ (68% CL). Curvature is constrained to $\sim 0.7\%$ in the owCDM model and to $\sim 2\%$ in a model in which dark energy is allowed to vary with parameters w_0 and w_a. Tightening further the constraints on the time evolution of dark energy will require several improvements, including high-quality multi-passband photometry of a sample of several dozen $z > 1$ SNe Ia. We describe how such a sample could be efficiently obtained by targeting cluster fields with WFC3 on HST.

The updated supernova Union2.1 compilation of 580 SNe is available at http://supernova.lbl.gov/Union

Subject headings: cosmology: general, supernovae: general, cosmological parameters, distance scale

[1] E.O. Lawrence Berkeley National Lab, 1 Cyclotron Rd., Berkeley, CA, 94720
[2] Department of Physics, University of California Berkeley, Berkeley, CA 94720
[3] Australian Astronomical Observatory, PO Box 296, Epping, NSW 1710, Australia
[4] The Oskar Klein Centre for Cosmo Particle Physics, AlbaNova, SE-106 91 Stockholm, Sweden
[5] Universidad Catolica de Chile
[6] Harvard-Smithsonian Center for Astrophysics, 60 Garden Street, Cambridge, MA 02138
[7] W. M. Keck Postdoctoral Fellow at the Harvard-Smithsonian Center for Astrophysics
[8] Hamilton College Department of Physics, Clinton, NY 13323
[9] Department of Physics and Astronomy, University of Utah, Salt Lake City, UT 84112
[10] National Optical Astronomy Observatory, Tucson, AZ 85726-6732
[11] Institute of Astronomy, Graduate School of Science, University of Tokyo 2-21-1 Osawa, Mitaka, Tokyo 181-0015, Japan
[12] Michigan State University, Department of Physics and Astronomy, East Lansing, MI 48824
[13] Space Telescope Science Institute, 3700 San Martin Drive, Baltimore, MD 21218

[14] Jet Propulsion Laboratory, California Institute of Technology, Pasadena, CA, 91109
[15] Center for Astrophysics and Space Astronomy, 389 UCB, University of Colorado, Boulder, CO 80309
[16] Santa Cruz Institute for Particle Physics, University of California Santa Cruz, Santa Cruze, CA 94064
[17] Department of Physics and Astronomy, University Of Waterloo, Waterloo, Ontario, Canada N2L 3G1
[18] Department of Astronomy and Astrophysics, University of Chicago, Chicago, IL 60637
[19] Department of Astronomy, University of Florida, Gainesville, FL 32611
[20] Department of Physics, Stockholm University, Albanova University Center, SE-106 91, Stockholm, Sweden
[21] School of Physics & Astronomy, University of Minnesota, Minneapolis, MN 55455
[22] Subaru Telescope, National Astronomical Observatory of Japan, 650 North A'ohaku Place, Hilo, HI 96720
[23] Leiden Observatory, Leiden University, Leiden, The Netherlands
[25] JSPS Fellow
[26] Department of Physics, University of California Davis, One Shields Avenue, Davis, CA 95616
[27] Department of Physics and Astronomy, Northwestern University, 2145 Sheridan Road, Evanston, IL 60208
[28] National Astronomical Observatory of Japan, 2-21-1 Osawa, Mitaka, Tokyo, 181-8588, Japan
[29] Kavli Institute for Cosmological Physics, The University of Chicago, Chicago, IL 60637
[30] Institute for Cosmic Ray Research, University of Tokyo, Kashiwa 277-8582, Japan

1. INTRODUCTION

More than a dozen years have passed since combined observations of nearby and distant Type Ia Supernovae (SNe Ia) demonstrated that the expansion of the Universe is accelerating at the current epoch (Perlmutter et al. 1998; Garnavich et al. 1998; Schmidt et al. 1998; Riess et al. 1998; Perlmutter et al. 1999). While the significance of the result has been boosted with the inclusion of larger, better calibrated SN Ia data sets (Knop et al. 2003; Astier et al. 2006; Wood-Vasey et al. 2007; Kowalski et al. 2008; Hicken et al. 2009b; Kessler et al. 2009; Guy et al. 2010) the cause of the acceleration remains unknown. Einstein's cosmological constant, for which w, the dark energy equation-of-state parameter, is exactly -1 and independent of time, is just one of several possible explanations that is consistent with the constraints from SNe Ia and the constraints from other probes, such as the Cosmic Microwave Background (CMB, Dunkley et al. 2009; Komatsu et al. 2011) and Baryon Acoustic Oscillations (BAO, Eisenstein et al. 2005; Percival et al. 2010).

SNe Ia constrain cosmological parameters through the comparison of their apparent luminosities over a range of redshifts. At the highest redshifts, $z > 1$, the Hubble Space Telescope (HST) has played and continues to play a key role, in discovering and confirming $z > 1$ SNe Ia (Riess et al. 2004, 2007; Kuznetsova et al. 2008; Dawson et al. 2009) and in providing high-precision optical and near-IR lightcurves. While constant w can be constrained using $z \sim 0.5$ SNe Ia, SNe Ia at $z > 1$ provide the necessary redshift baseline to constrain time-varying w and some astrophysical systematics like intergalactic dust (Ménard et al. 2010).

Discovering and following distant SNe Ia with the HST requires substantial amounts of telescope time because the field-of-view is quite small compared to that of ground-based telescopes. Therefore, all HST SN Ia discovery programs have coupled the search for SNe Ia and their photometric follow-up with other scientific studies. The GOODS survey (Dickinson et al. 2003; Riess et al. 2004, 2007; Kuznetsova et al. 2008) is an example that provided a window to probe the high-z universe for studying galaxy evolution (e.g. Beckwith et al. 2006; Bouwens et al. 2006; Bundy et al. 2005) in addition to $z > 1$ SNe. Nevertheless, progress in building a large sample of $z > 1$ SNe Ia discov-

ered with HST is slow. In the most recent SN Ia compilation (Union2, Amanullah et al. 2010) which consists of 557 SNe after the lightcurve quality cuts, only 16 HST-discovered $z > 1$ SNe Ia were available to help constrain a time-evolving w. (Well measured ground-based $z > 1$ SNe account for an additional four.)

Targeting regions that are rich in potential SN Ia hosts, such as galaxy clusters, offers a more effective strategy for using HST for SN Ia studies. Some of the earliest SN Ia searches used this strategy when the field-of-view of ground-based images were only a few arc minutes across. The first spectroscopically confirmed high-redshift SN Ia was discovered in a galaxy cluster (SN1988U: z=0.31, Norgaard-Nielsen et al. 1989) as was the first high-redshift SN Ia observed by HST (SN1996cl: z=0.83, Perlmutter et al. 1998, 1999). However, the advent of large-format CCDs, CCD mosaics and imagers with wide fields of view quickly led away from this approach in the late 80's and early 90's (Perlmutter et al. 1991).

Given the large increase in the number of very distant clusters that have been discovered over the last 10 years, the angular extent of these clusters, and the field-of-view that is available with HST, targeting galaxy clusters beyond $z \sim 1$ is again an effective strategy. In this paper, we discuss results from our HST Cluster SN survey obtained using this strategy. In addition to increasing the yield of SNe Ia discoveries per HST orbit by a factor of two (Dawson et al. 2009), we increase the yield of SNe Ia in early-type galaxies by a factor of approximately four (Meyers et al. 2011).

SNe Ia hosted by early-type galaxies offer several potential advantages over SNe Ia found in a broader range of host types. Stars in early-type galaxies are considerably older and span a smaller mass range than stars in late-type hosts. This may lead to a more uniform progenitor population. Evidence for this can be seen in the distribution in light curve widths. SNe Ia in early-type host galaxies follow a narrower distribution than SNe Ia in late-type galaxies (Hamuy et al. 1996, 2000; Riess et al. 1999; Sullivan et al. 2006). Interestingly, the relationship between SN Ia color and host galaxy type is weak (Sullivan et al. 2010). Using data from the HST Cluster SN Survey, we confirm both of these relationships for $z > 1$ SNe Ia in Meyers et al. (2011).

With the availability of larger, better-calibrated samples, evidence for a correlation between host galaxy properties and SN Ia luminosities after corrections for lightcurve width and SN Ia color is now emerging. Hicken et al. (2009c) found that SNe Ia in early-type galaxies (morphologically classified as E and S0 galaxies), are 0.14 ± 0.07 mag brighter after lightcurve shape and color corrections than SNe Ia in galaxies of later types. A relationship of roughly the same significance between host galaxy mass[1] and Hubble residuals was reported by Kelly et al. (2010), Sullivan et al. (2010) and Lampeitl et al. (2010). Uncorrected, this relationship leads to a significant systematic error in determining cosmological parameters, as the fraction of SN Ia in galaxies with high specific star-formation rates increases with increasing redshift (Sullivan et al. 2010). We expect that the host mass correction is a proxy for more profound physics behind the SN Ia explosion mechanism; SNe Ia in early-type galaxies may lead to a better understanding of this correlation, given that more accurate mass, metallicity and age can be assigned to early-type galaxies (Bruzual & Charlot 2003; Tremonti et al. 2004;

[31] Physikalisches Institut Universität Bonn, Germany

[32] Astronomy Department, University of Washington, Seattle, WA 98195

[33] Wachovia Corporation, NC6740, 100 N. Main Street, Winston-Salem, NC27101

[34] Department of Astronomy, Kyoto University, Sakyo-ku, Kyoto 606-8502, Japan

[35] Astronomy and Astrophysics, The Pennsylvania State University, University Park, PA 16802

[36] California Institute of Technology, Pasadena, CA 91125

[37] ESO, Karl-Schwarzschild-Strasse 2, D-85748 Garching, Germany

[38] Institute of Geophysics and Planetary Physics, Lawrence Livermore National Laboratory, Livermore, CA 94550

[39] CENTRA - Centro Multidisciplinar de Astrofísica, Instituto Superior Técnico, Av. Rovisco Pais 1, 1049-001 Lisbon, Portugal

[40] Space Sciences Lab, 7 Gauss Way, Berkeley, CA 94720

[41] Department of Physics, Texas A & M University, College Station, TX 77843, USA

[42] Institute for the Physics and Mathematics of the Universe, University of Tokyo, Kashiwa, 277-8583, Japan

[43] Department of Astronomy and Astrophysics, University of Toronto, Toronto, ON M5S 3H4, Canada

[44] Deceased

[1] Host galaxy metallicity, specific-star-formation rate, or age are also drivers, as these quantities are somewhat degenerate in current data.

Maraston 2005).

An additional source of astrophysical uncertainty concerns the color correction that is applied to SN Ia luminosities. There appears to be at least two mechanisms for the redder-fainter relation: extinction from dust in the ISM, which must play a role at some level, and an intrinsic relation between color and luminosity due to the explosion itself or the surrounding environment. There is no reason to believe that the redder-fainter relationship should behave in the same way for both mechanisms at all redshifts, but the two effects have proven to be hard to disentangle.

Early-type galaxies contain significantly less dust than late-type galaxies, so separating SNe Ia according to early and late types offers a way to study the intrinsic component and to perhaps estimate the relative contribution and importance of dust in a broader sample. An early-type only sample may also yield a Hubble diagram with smaller statistical errors. Early work, based on a few dozen SNe Ia without color correction, suggested that SNe Ia in early-type galaxies are better standard candles (Sullivan et al. 2003). The evidence from more recent works, which use larger samples and better data, revealed that SNe Ia exhibit intrinsic diversity in color, but support the original findings (Sullivan et al. 2003) with lower statistical significance (Sullivan et al. 2010).

Per unit stellar mass, SNe Ia are far less common in passive, early-type galaxies than in star forming, late-type galaxies (Mannucci et al. 2005; Sullivan et al. 2006). Depending on the way hosts are classified, about one in five SNe Ia at low redshift will be hosted by an early-type galaxy. At higher redshifts, the fraction is expected to decrease, due to a combination of an increase in the amount of star formation and observational selection biases. Galaxy clusters, which are rich in early-type galaxies, even up to $z \sim 1.4$, are an effective way of finding SNe Ia in early-type hosts (Dawson et al. 2009).

This paper is one of a series of ten papers that report supernova results from the HST Cluster Supernova Survey (PI: Perlmutter, GO-10496), a survey to discover and follow SNe Ia of very distant clusters. Paper I (Dawson et al. 2009) describes the survey strategy and discoveries. Paper II (Barbary et al. 2010) reports on the SN Ia rate in clusters. Paper III (Meyers et al. 2011) addresses the properties of the galaxies that host SNe Ia. Paper IV (Ripoche et al. 2011) introduces a new technique to calibrate the "zeropoint" of the NICMOS camera at low counts rates, which is critical for placing NICMOS-observed SNe Ia on the Hubble diagram. The current work, Paper V, reports the SN Ia lightcurves and cosmology from the HST Cluster SN Survey program. Paper VI (Barbary et al in prep) will report on the volumetric field SN Ia rate. Melbourne et al. (2007), one of several unnumbered papers in this series, present a Keck Adaptive Optics observation of a $z = 1.31$ SN Ia in H-band. Barbary et al. (2009) report the discovery of the extraordinary luminous supernova, SN SCP06F6. Morokuma et al. (2010) presents the spectroscopic follow-up observations for SN Ia candidates. Hsiao et al. (2011) develop techniques to remove problematic artifacts remaining after the standard STScI pipeline. A separate series of papers, ten to date, reports on cluster studies from the HST Cluster SN Survey: Brodwin et al. (2010); Eisenhardt et al. (2008); Jee et al. (2009); Hilton et al. (2007, 2009); Huang et al. (2009); Santos et al. (2009); Strazzullo et al. (2010); Rosati et al. (2009); and Jee et al. (2011).

This paper is organized as follows. In §2, we describe the HST Cluster SN Survey, the search strategy and discuss SN Ia typing. In §3, we describe the procedures we used to process data and present the SN Ia photometry. In §4, we update the Union2 sample by adding the new SNe Ia from this paper, and we use the revised compilation to constrain cosmological parameters in §5.

2. SN DISCOVERIES AND DATA

The HST Cluster Supernova Survey targeted 25 high-redshift galaxy clusters in the redshift range $0.9 < z < 1.5$ with the ACS camera on HST. Clusters were selected from the IRAC Shallow Cluster Survey (Eisenhardt et al. 2008), the Red-Sequence Cluster Surveys (RCS and RCS-2, Gladders & Yee 2005; Gilbank et al. 2010), the XMM Cluster Survey (Sahlén et al. 2009), the Palomar Distant Cluster Survey (Postman et al. 1996), the XMM-Newton Distant Cluster Project (Bohringer et al. 2005), and the ROSAT Deep Cluster Survey (RDCS, Rosati et al. 1999). At the time we conducted our survey, the sample represented a significant fraction of the known $z > 0.9$ clusters. Here, we summarize the SNe discovered in our survey.

2.1. SN Sample

As described in Dawson et al. (2009), the survey produced a total of 39 likely SNe during the active phase of the search. In Barbary et al. (2010), types are determined for 29 of these candidates. (The remaining 10 do not have enough light curve information to determine type, since they lie outside of our fiducial search time window or our signal-to-noise cuts.) Twenty SNe are classified as SNe Ia, with confidence levels of secure, probable or plausible. A secure SN Ia is one that either has a spectrum that directly confirms it to be a SN Ia or one that satisfies two conditions: (1) it occurred in a host whose spectroscopic, photometric and morphological properties are consistent with those of an early-type galaxy with no detectable signs of recent star formation, and (2) it has a lightcurve shape consistent with that of a SN Ia and inconsistent with all other known SN types. A probable SN Ia is one that does not have a secure spectrum but satisfies one of the two non-spectroscopic conditions that are required for a secure classification. A plausible SN Ia is one that has an indicative lightcurve but we do not have enough data to rule out other types. Details of the classification scheme can be found in Barbary et al. (2010), and details of the galaxy typing can be found in Meyers et al. (2011).

Sixteen SNe are classified as either secure or probable. We use these SNe in the cosmological analysis. We include the photometry and lightcurves of an additional four plausible SNe Ia to illustrate the quality of the data and the potential for a similar sample with complete classification (and because additional host galaxy data may later bring one of these into the larger sample). Secure, probable and plausible SN Ia are listed in Table 1, together with their position, redshift and typing. Postage stamp images of the SNe and host galaxies are shown in Figure 1.

We labeled each of our 25 clusters with a letter from 'A' to 'Z' (excluding 'O' to avoid confusion with zero) and assigned supernova names as 'SCP'+[discovery year]+ [discovered cluster]+[SN ID]. The cluster IDs, coordinates, and redshifts are found in tables in Dawson et al. (2009); Barbary et al. (2010); Meyers et al. (2011). The cluster membership is discussed in Meyers et al. (2011) in detail and summarized in Table 1 along with host type information.

Several SNe Ia deserve special mention:

Table 1
Supernova from HST Cluster Supernova Survey

SN name	Nickname	z^{b}	$z_{\mathrm{cluster}}^{\mathrm{c}}$	RA (J2000)	DEC (J2000)	E(B-V)$^{\mathrm{d}}$	Confidence
				SNe Hosted by Cluster Early-Type Galaxies			
SCP05D0$^{\mathrm{a}}$	Frida	1.014	1.017	02:21:42.066	−03:21:53.12	0.025	secure
SCP06H5	Emma	1.231	1.241	14:34:30.140	+34:26:57.30	0.019	secure
SCP06K0	Tomo	1.415	1.414	14:38:08.366	+34:14:18.08	0.015	secure
SCP06K18	Alexander	1.411	1.414	14:38:10.665	+34:12:47.19	0.014	probable
SCP06R12	Jennie	1.212	1.215	02:23:00.083	−04:36:03.05	0.026	secure
SCP06U4$^{\mathrm{a}}$	Julia	1.050	1.037	23:45:29.430	−36:32:45.75	0.014	secure
				SNe Hosted in the Cluster			
SCP06C1$^{\mathrm{a}}$	Midge	0.98	0.974	12:29:33.013	+01:51:36.67	0.019	secure
SCP06F12	Caleb	1.110	1.110	14:32:28.749	+33:32:10.05	0.010	probable
				SNe Hosted by Early-Type Non-Cluster Members			
SCP05D6	Maggie	1.315	1.017	02:21:46.484	−03:22:56.18	0.025	secure
SCP06G4$^{\mathrm{a}}$	Shaya	1.350	1.259	14:29:18.744	+34:38:37.39	0.015	secure
SCP06A4	Aki	1.192	1.457	22:16:01.078	−17:37:22.10	0.026	probable
SCP06C0	Noa	1.092	0.974	12:29:25.655	+01:50:56.59	0.020	secure
				SNe Hosted by Late Type Galaxies			
SCP06G3	Brian	0.962	1.259	14:29:28.430	+34:37:23.15	0.015	plausible
SCP06H3$^{\mathrm{a}}$	Elizabeth	0.850	1.241	14:34:28.879	+34:27:26.62	0.019	secure
SCP06N33	Naima	1.188	1.026	02:20:57.699	−03:33:23.98	0.023	probable
SCP05P1	Gabe	0.926	1.1	03:37:50.352	−28:43:02.67	0.011	plausible
SCP05P9$^{\mathrm{a}}$	Lauren	0.821	1.1	03:37:44.513	−28:43:54.58	0.011	secure
SCP06X26	Joe	1.440	1.101	09:10:37.888	+54:22:29.06	0.019	plausible
SCP06Z5$^{\mathrm{a}}$	Adrian	0.623	1.390	22:35:24.967	−25:57:09.61	0.021	secure
				SNe with No Definitive Redshift Measurement			
SCP06E12	Ashley	$\cdots$	1.026	14:15:08.141	+36:12:42.93	0.009	plausible

$^{\mathrm{a}}$ Spectroscopically confirmed as a SNe Ia
$^{\mathrm{b}}$ Redshift from SNe Ia or host galaxy (Morokuma et al. 2010, Barbary et al. 2010, Meyers et al. 2011)
$^{\mathrm{c}}$ Redshift from cluster (Meyers et al. 2011, references therein)
$^{\mathrm{d}}$ Galactic Extinction from Schlegel et al. (1998)

SN SCP06C1, a supernova discovered in 2006 in cluster C (XMMU J2205.8−0159) and numbered as '1' among other transient candidates, could not be clearly associated with a galaxy in the cluster but was spectroscopically confirmed as a SN Ia at the cluster redshift. It might be an example of a SN Ia that comes from a progenitor in the intracluster stellar population (Sand et al. 2010). SN SCP06C1 is discussed in greater detail in Barbary et al. (2010). As there was a bright background galaxy near the position of the supernova, had we not obtained a spectrum of the supernova, we would have misidentified the redshift. We note that experiments that do not obtain spectroscopy of their supernovae and instead assume the nearest visible galaxy is the host will have to factor cases like SN SCP06C1 into their analyses.

SN SCP05D6, SN SCP06G4, and SN SCP06N33 occur behind the cluster, and are therefore gravitationally lensed by the cluster. In most surveys, the lensing for SNe Ia hosted by field galaxies averages to nearly zero. In this survey, we target regions with larger than average magnification, so we must make the correction for SNe behind the clusters. To estimate the amount of magnification, we use the virial mass, M_{200}, from our weak lensing measurements (Jee et al. 2011). We assume a spherical Navarro-Frenk-White profile (NFW; Navarro et al. 1997) with the concentration parameters determined by the $M_{200} - c$ relation in Duffy et al. (2008). The lensing magnifications for SN SCP05D6, SN SCP06G4 and SN SCP06N33 are esti-

mated to be $1.021^{+0.012}_{-0.008}$, $1.015^{+0.005}_{-0.004}$ and $1.066^{+0.017}_{-0.014}$ respectively. The magnification of SN SCP06N33 is larger than the others because the cluster is massive, and the host galaxy is located at approximately half the distance from cluster center as the others. We apply these corrections when using these SNe Ia in the cosmological fits and propagate the uncertainties accordingly.

SN SCP06C0 is a more interesting case. The host is also behind the lensing cluster, which means that SN SCP06C0 will be lensed as well. Following the methodology used to correct SN SCP06G4, SCP SN05D6 and SCP SN06N33, we find the magnification of SN SCP06C0 to be $1.030^{+0.007}_{-0.005}$. Upon closer inspection of the host in the stacked ACS data and in more recent WFC3 data, a second much fainter object, projected only $0.\!''6$ from the center of the host and about $0.\!''2$ from SN SCP06C0, was detected. The object could be a satellite of the host, or it could be an unrelated galaxy along the line of sight. A spectrum of SN SCP06C0 was taken when it was about 6 days after maximum light; however, the signal-to-noise ratio was insufficient to allow a clear detection of light from the supernova given the observing conditions and the relative brightnesses of the hosts and the supernova. The classification and redshift therefore rely on correctly assigning the supernova to the brighter galaxy. In § 3.2.3, we model the surface brightness distribution of both galaxies. At the location of the supernova, the surface brightness of the large galaxy is four times greater than the surface brightness of the
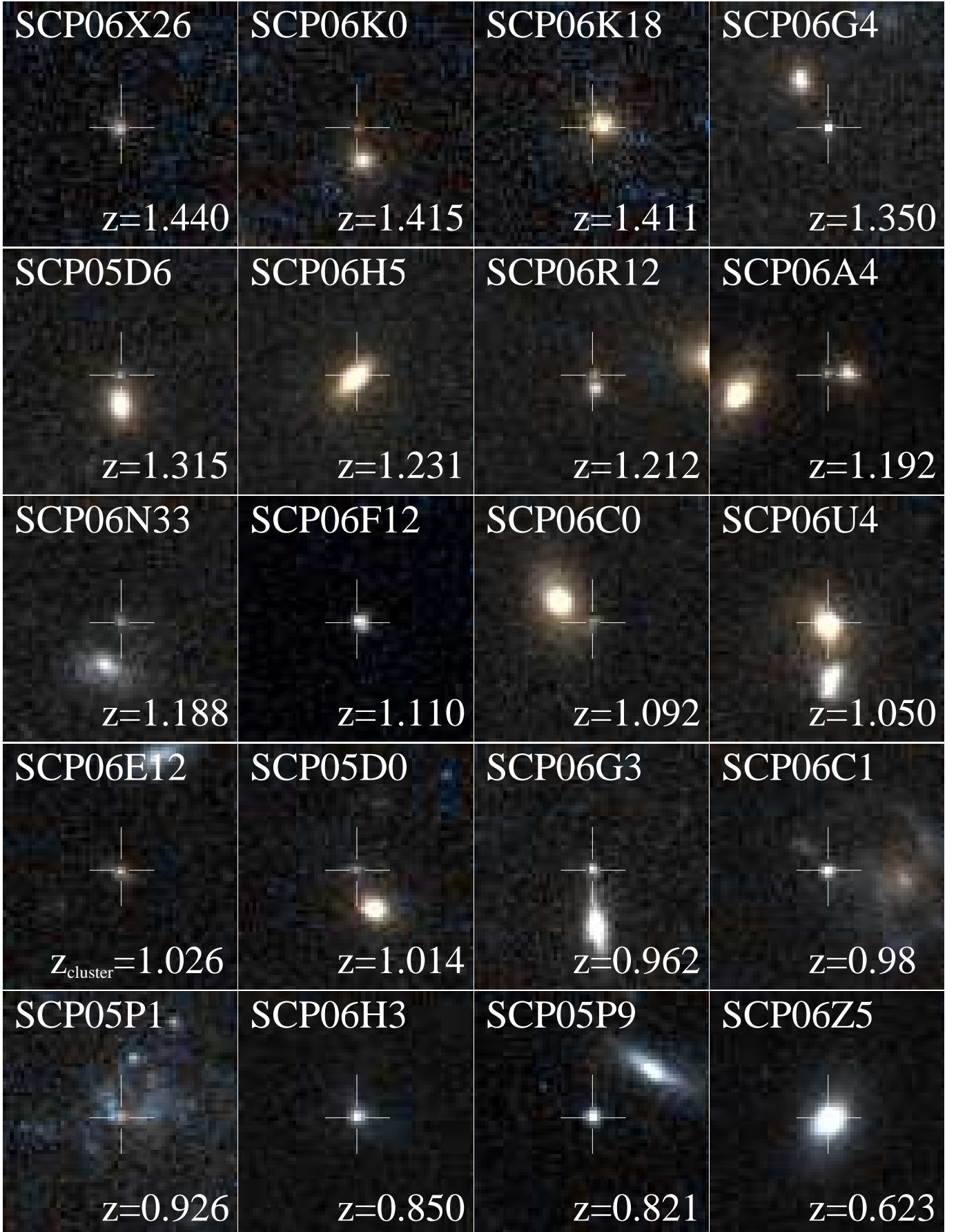
Figure 1. Composite color (i_{775} and z_{850}) images of 20 SNe Ia from the HST Cluster Supernova Survey. Each SN Ia is shown in a box of $3.2'' \times 3.3''$ (North up and East left). Note the redshift of SCP06E12 is uncertain, and we use the cluster redshift as a guide.

small galaxy. Since [OII] was not detected in spectra that were taken after the supernova had faded from view, neither galaxy is actively forming stars. The relative supernova rate is therefore directly related to relative surface mass density of the the two galaxies. Using the surface brightness as a proxy for the surface mass density, we therefore assign SN SCP06C0 to the larger of the two galaxies with $\sim 80\%$ confidence and include this SNe Ia in the cosmological fits.

3. PHOTOMETRY

In this section, we describe the steps that were used to process the ACS and NICMOS data after they had been processed with the standard STScI pipelines. For the ACS data, we removed the spatially variable background from the pipeline processed data and applied charge transfer efficiency (CTE) and red-halo scattering corrections to the extracted fluxes. For the NICMOS data, we processed the data to compensate for amplifier offsets, bright Earth persistence, contamination from the passage of the telescope through the South Atlantic Anomaly (SAA), residual amplifier glow and fringing, and applied a wavelength-dependent non-linearity correction. A more detailed description of the individual steps now follows.

3.1. *ACS Processing and Photometry*

In general, the search consisted of four z_{850} exposures per epoch and a single i_{775}-band exposure. All exposures are geometrically corrected (and multiple exposures are stacked) using MultiDrizzle (Fruchter & Hook 2002; Koekemoer et al. 2002). The photometry is performed on the stacked z_{850}-band image and the single i_{775}-band drizzled image. In addition to the data that were taken during the search, five clusters, CL1604+4304 (Postman et al. 2005), RDCS0910+54 (Mei et al. 2006), RDCS0848+44 (Postman et al. 2005), RDCS1252−29 (Blakeslee et al. 2003) and XMMU2235.3−2557 (Jee et al. 2009) were observed with ACS prior to our program (PID9290 and PID9919). We have included all these data and processed them and the search data in a uniform way. In total, 1006 ACS exposures were processed.

After processing the ACS data with the standard STScI pipeline using the most up-to-date calibration files, we removed the spatially variable background by masking all objects and artifacts, and subtracting a heavily smoothed, median version of what remained. Given the time baseline of our observations, guide stars changed between epochs. We must therefore use objects in the images - typically 20 to 30 objects per image - to tie the relative astrometry between epochs. The size of the residuals was typically 0.2 pixels, which is larger than one usually expects from point sources with good signal-to-noise ratios. We attribute this to temporal and spatial uncertainties in the distortion correction that are applied to images that are both temporally separated by many months and rotated with respect to one another (Anderson 2007). The absolute astrometry is tied to the Guide Star Catalogue, version 2.3.2 [1], and has an uncertainty of $0.3''$.

We use apertures of 3-pixel radius to measure fluxes and report the i_{775} and z_{850} photometry for each epoch of each SN in the electronic version of this paper. An example is shown in Table 2. The background noise is found empirically by randomly placing apertures within regions that are free of objects and then measuring the dispersion in the integrated counts within these apertures. We have compared the signal-to-noise ratios obtained for aperture and PSF photometry and found that the difference between the two is small if we use such small apertures. We use aperture photometry here, as it allows for a more robust correction of CTE and red halo scattering (described below).

The photometry is corrected for variable CTE and for flux that is outside the aperture (referred to here as the aperture correction). CTE depends on the position of the source, the level of the background sky and the flux of the object that is being corrected. It also degrades with time. We follow the formulation of Riess & Mack (2004) and apply the correction factor that corresponds to the 3-pixel radius case and the dates of our observations. On average, we applied a 4.3% correction to the SN Ia flux. When calculating CTE corrections, we include the local background that had been previously subtracted.

We also apply a color-dependent aperture correction on the ACS z_{850}-band measurements. In ACS z_{850}-band data, long-wavelength photons scatter off the back-side of the CCD, causing a degradation in the PSF. The effect is commonly known as red-halo scattering (Sirianni et al. 1998). The Tiny-Tim[2] PSF does not account for this effect, hence it does not reproduce the observed z_{850}-band PSF. We studied how the PSF changes with wavelength using standard stars taken with a series of narrow-band filter observations from HST calibration programs PID9020 and PID10720. We measured the red-halo scattering correction factor as a function of aperture radius and wavelength. For a given aperture, we then can treat the correction as a modification of the F850LP throughput and zeropoint. We discuss the details of this procedure in the Appendix.

We have used the updated STScI ACS Vega zeropoints for light curve fitting. The latest zeropoints are from the STScI web site[3] which were posted on May 19th, 2009. The ACS zeropoints changed on July 4th, 2006 due to a change in the detector temperature. The STScI definition assigns Vega (α Lyr) a magnitude of 0.0 in every filter. However, in the Landolt system, which the SN Ia photometry in the literature refers to, Vega is not zero. To be consistent with literature SNe Ia, we introduce this non-zero Vega magnitude correction to our zeropoints. For both the i_{775} and z_{850}-bands, the correction is 0.024 mag (Fukugita et al. 1996). We therefore adjust the STScI zeropoints by this amount (Astier et al. 2006), and use Vega zero points of $i_{775} = 25.291(\text{STScI})+0.024 = 25.315$ and $z_{850} = 24.347(\text{STScI})+0.024 = 24.371$ for data taken before July 2006 (corresponding to a detector temperature of -77C), and $i_{775} = 25.277(\text{STScI})+0.024 = 25.301$ and $z_{850} = 24.323(\text{STScI})+0.024 = 24.347$ for data taken after July 2006 (corresponding to a detector temperature of -81C).

3.2. *NICMOS Processing and Photometry*

All NICMOS science frames were processed with the latest CALNICA pipeline (version 4.4.1 Dahlen et al. 2008) and then corrected for three well-known anomalies: the offset between amplifiers, which affects all NICMOS exposures and is removed using the STSDAS PyRAF task PEDSKY; persistence after passage of the telescope through the South Atlantic Anomaly (SAA); and persistence after exposing the detectors to the limb of the Earth. Nine exposures are affected by the SAA, which leaves persistent signals from SAA cosmic rays. We applied the STSDAS PyRAF task SAACLEAN

Table 2
Photometry Data

SN name	Instrument	Filter	MJD	Flux[a] (counts/s)	Flux Error[a] (counts/s)	Vega Zeropoint [d]	Exptime (s)	Nexp[b]	Raw Flux[c] (counts/s)	Raw Flux Error[c] (counts/s)
SCP05D0	ACS	F850LP	53564.098	-0.0283	0.0547	24.371	2000	4	-0.0188	0.0365
SCP05D0	ACS	F850LP	53589.117	0.7733	0.0573	24.371	2000	4	0.5153	0.0381
SCP05D0	NICMOS	F110W	53604.074	0.5092	0.0230	23.029	2560	2	⋯	⋯
SCP05D0	ACS	F850LP	53610.836	1.5084	0.0649	24.371	2000	4	1.0040	0.0432
SCP05D0	ACS	F850LP	53633.184	0.7290	0.0704	24.371	1500	4	0.4764	0.0460
SCP05D0	ACS	F775W	53633.215	0.7989	0.2229	25.315	375	1	⋯	⋯
SCP05D0	ACS	F850LP	53654.434	0.2388	0.0694	24.371	1500	4	0.1520	0.0442
SCP05D0	ACS	F775W	53654.469	0.3908	0.1725	25.315	375	1	⋯	⋯
SCP05D0	ACS	F850LP	53679.258	0.1792	0.0708	24.371	1500	4	0.1137	0.0450
SCP05D0	ACS	F775W	53679.273	-0.1432	0.1823	25.315	375	1	⋯	⋯
SCP05D0	ACS	F850LP	53704.266	0.0279	0.0715	24.371	1500	4	0.0174	0.0446
SCP05D0	ACS	F775W	53704.305	0.0624	0.2072	25.315	375	1	⋯	⋯
SCP05D0	ACS	F850LP	53965.207	0.0356	0.0738	24.347	1360	4	0.0216	0.0448
SCP05D0	ACS	F775W	53965.246	-0.0034	0.1981	25.301	515	1	⋯	⋯

Note. — The complete set of SNe Ia photometry data is available in its entirety in the electronic edition of the *Astrophysical Journal*. A portion is shown here for guidance regarding its form and content.

[a] Flux, corrected for CTE and color-dependent aperture correction (for ACS) and the count rate non-linearity (for NICMOS). For the ACS F850LP filter, z_{850}, this is the result of the iterative Method I in Appendix A

[b] The number of exposures.

[c] CTE corrected but not aperture-corrected flux for the ACS F850LP data. This flux column is used as an input for the modified filter Method II in Appendix A. Note we use the modified filter response curve and shifted zeropoint as described in Appendix A

[d] The zeropoint has changed slightly after July 4th, 2006 (MJD=53920) due to the change in detector temperature.

(Barker et al. 2007) to remove SAA persistence effects from the images. When a NICMOS observation is immediately preceded by an ACS data dump, the process could delay the NICMOS placement of the filter blank, subjecting the detectors to the bright limb of the Earth, which imprints a persistent pattern on subsequent exposures (Riess & Bergeron 2008). Four exposures were affected in this way and were corrected using the STSDAS software NIC_REM_PERSIST. At this point, the mode of the flux distribution in each image is measured and recorded. These values are used as the sky levels for the count-rate non-linearity correction.

Even after correcting NICMOS data for these well-studied anomalies, significant large-scale background non-uniformities remain. We developed methods to extract and remove the background structures; these are detailed in Hsiao et al. (2011). Briefly, the models for the background structures are studied and characterized using approximately 600 NICMOS exposures observed through the F110W filter and processed with the procedures described above. Principal component analysis applied on these images revealed that the intensity of the residual corner amplifier glow depends on the exposure sequence. The amount of residual glow decays exponentially and resets every orbit. With exposure times on the order of 1000 seconds, the exposures can be separated into two glow groups, each with approximately constant intensity. This makes it possible to extract the residual glow algebraically. The structured background is modeled as a combination of a constant component and a component that scales with the sky level and exposure time. The models are derived from the algebraic manipulation of stacked images for each glow group. The resulting constant component of the model is dominated by residual amplifier glow at the corners and residual persistence structure at the center. The model component which scales with sky level and exposure time displays a curious fringe pattern whose origin is unknown. The model components are fit to individual exposures via scale parameters to create the customized background models to be subtracted from the individual exposures. In a final step, the bias offsets

apparent in the middle column and middle row are removed. Additional details can be found in Hsiao et al. (2011).

3.2.1. *NICMOS Count-rate non-linearity*

The NICMOS data are critically important for measuring the color of $z > 1$ SNe Ia. Any uncertainty in the NICMOS calibration severely limits the usefulness of SNe Ia observed with NICMOS. In particular, the NIC2 detector exhibits a count-rate dependent non-linearity (Bohlin et al. 2005), the severity of which is a function of wavelength.

This non-linearity previously has only been studied at count rates three orders of magnitude higher (de Jong et al. 2006) than the count rate of a typical SN Ia at $z = 1$, meaning that correcting the flux of SN Ia at $z = 1$ requires significant extrapolation and has a level of uncertainty that is difficult to quantify. For example, comparisons between ground-based near-IR data and a different NICMOS camera (NIC3) showed that little or no correction is required for that camera (Mobasher & Riess 2005). It is difficult to reconcile this finding with the findings of Bohlin et al. (2006) and de Jong et al. (2006). A simple test at the flux levels relevant for the supernovae in this paper shows a difference of 12% between NIC2 and NIC3 when the non-linearity corrections are made, revealing significant problems with these extrapolations.

For the NIC2/F110W filter, the degree of count-rate non-linearity is ~ 0.06 mag per factor of 10 change in count rate (Bohlin et al. 2006; de Jong et al. 2006). The count rates from stars that are used to determine the NICMOS zero points are five orders of magnitude higher than the count rate of a typical SN Ia at $z = 1$. This corresponds to a ~ 0.3 mag correction for the NIC2/F110W filter!

Since this is so important to the cosmological results, we have developed a method to address this count-rate non-linearity calibration directly (Ripoche et al. 2011). We analyze ACS, NICMOS, and ground-based near-IR observations of early-type galaxies from clusters RCS J0221.6−0347 ($z = 1.02$), RDCS J1252.9−2927 ($z = 1.24$), and XMMU J2235.3−2557 ($z = 1.39$). The space and ground-based

data are used to constrain the spectral energy distributions (SED) of these galaxies, which are then numerically integrated through the F110W filter transmission curve and compared to the counts measured with NICMOS. The principle advantage of the technique is that the count rate from early type galaxies at this redshift is similar to that measured for SNe Ia, i.e. about 0.03 counts/second/pixel (the contribution from amplifier glow is comparable). We applied this technique using three galaxy clusters that have deep ground based near-IR imaging data from the VLT and deep images with the ACS and NICMOS camera. All three clusters are at different redshifts and produced consistent results. At the low count rates that are applicable to high-redshift SNe Ia, we find that the prescription of Bohlin (2007) and de Jong et al. (2006) over-predicts the zeropoint correction for the NIC2 camera with the F110W filter by 0.065 mag. We therefore use our zeropoint of 23.029 (Vega magnitude) or 23.757 (AB magnitudes). Additional details can be found in Ripoche et al. (2011).

At high count rates, the count-rate non-linearity size has a strong dependence with wavelength across filters (de Jong et al. 2006), being considerably stronger in bluer filters. The SED of an early-type galaxy at $z \sim 1.2$, is a good match to a SN Ia about 20 rest-frame days after maximum, but is redder than a supernova SED at maximum (though this is compensated somewhat by the fact that the background level is about 1/3 of the source flux and is blue in the F110W bandpass). The size of the count-rate non-linearity correction will thus also depend weakly on the phase and redshift, varying from 0.02 magnitudes at maximum to no additional correction 20 rest-frame days after maximum. Since the wavelength-dependence of the non-linearity may not be even this strong at low count rates, we apply half the correction applicable at each phase, and add (in quadrature) an additional 0.01 magnitudes to the F110W zeropoint error to account for this uncertainty. When added to the 0.006 mag statistical error, and 0.021 mag systematic error (Ripoche et al. 2011), this gives a total uncertainty on the zeropoint of 0.024 magnitudes. For the GOODS supernovae with NICMOS observations, we start with the original flux given by Riess et al. (2007) (after converting the magnitude measurements to fluxes using the given zeropoint of 22.92), but increase the flux by 0.01 magnitudes, representing half the correction for the (possible) wavelength-dependence of the count-rate non-linearity.

3.2.2. *Galaxy Models*

After the postprocessing described above (Hsiao et al. 2011), we measure fluxes from the eight SNe Ia with NICMOS observations by performing PSF photometry on the images. In all cases, the SNe Ia are not separated enough from their hosts to allow us to fit for the supernova flux alone; rather we fit a model of the host galaxy as well. By performing PSF photometry using analytic galaxy models, we avoid re-sampling the images (the better PSF sampling for the ACS data negates this advantage of PSF photometry), and extract the maximum possible signal-to-noise from our observations. We fit an analytic model of the host galaxy even when we have reference images, as this gives higher signal-to-noise, and nearly uncorrelated photometry between epochs[1].

Model PSFs for the supernovae are obtained with the TinyTim software using supernova SED templates from Hsiao et al. (2007) redshifted to the supernova redshift and warped as a function of wavelength to match the photometry. After the lightcurve fitting is complete, new PSFs are generated from the SEDs based on this photometry and the process is repeated. Model PSFs for the galaxies are obtained with TinyTim by appropriately redshifting a galaxy spectrum from Bruzual & Charlot (2003) with an age of $2.5 \, \mathrm{Gyr}$ and a solar metallicity; the exact shape of the galaxy spectrum does not greatly affect the results. The PSFs used are $3''$ in diameter, comparable to the patch fit in each NICMOS image.

Although there is virtually no information at scales smaller than about half a pixel, all PSFs are seven times oversampled. This oversampling is necessary because the PSF is made slightly wider by the convolution with the subsampled pixels, increasing the flux of the derived photometry. In order for this effect to be negligible, seven times oversampling must be used. Finally, a correction is made to match the photometry from the $3''$ TinyTim PSFs to the $30''$ TinyTim PSFs used in Ripoche et al. (2011). These differently-sized PSFs show different structure far in the wings, but the flux in the core changes by 3.5%, with negligible variation.

We generally model the host galaxies as ellipsoids, with radial profiles given by second degree polynomial splines. These splines have ten nodes, with spacing that asymptotically approaches an exponential away from the core. The higher node density near the core provides more freedom to model the host where the flux changes quickly with position. In the few pixels closest to the core, where the spline changes rapidly, we numerically integrate over each subpixel before convolving with the PSF. On the basis of our tests (see §3.2.3), the hosts of some supernovae were modeled with modifications to this basic scheme, as discussed in the following section.

3.2.3. *Photometry Testing*

Three ingredients all have to be correct in order to achieve photometry with low bias and variance: the PSF model, the galaxy model, and the supernova centroid. Deriving a PSF from a field star (details in the SN SCP06C0 discussion below) and comparing against TinyTim gives photometry consistent to a few mmags, so we do not believe this is a major contribution to our errors.

Testing the host galaxy model and supernova centroiding is more involved. For each observation, we subtract the best-fit supernova light, and place simulated supernovae (at the same flux level) in the images. The only place one cannot do this test is at the location of the actual supernova, as putting a simulated PSF in this location yields a measurement that will be highly correlated with the measurement of the supernova. We therefore do not place any simulated supernovae closer than two pixels to the best-fit location of the supernova. By examining the bias and variance of the extracted fluxes from a large number of simulations (~ 100), we can choose the galaxy model which gives the most precise and accurate[2] fluxes for each particular supernova. We emphasize that the results of these simulations were the only metric used in choosing the detailed model. In particular, there was no feedback from the shape of the lightcurve or the Hubble diagram since these would have undercut the principles of "blind" analysis we

---

[1] Had we subtracted the flux in the reference images at the location of the supernova, the errors from this flux would have to be propagated as a covariance for all the other epochs. The errors on the galaxy model at the position of the supernova are typically much smaller.

[2] We found that precision and accuracy correlated in our simulations.

tried to maintain (see §4). The same basic galaxy model (discussed above) was used for the NICMOS photometry of each supernova, with the following exceptions.

- SN SCP06C0: As mentioned in §2.1, there is a small galaxy about $0.6''$ from the likely host of SN SCP06C0, and just $0.2''$ from SN SCP06C0 itself. We note that the surface brightness of the small galaxy is one fourth of that host at the location of the supernova. The host also has some azimuthal asymmetry visible, indicating a possible merger. The cluster XMM1229+01 was also observed as part of a program to cross-calibrate NICMOS (Ripoche et al. in preparation) and deep, well-dithered images were obtained in the WFC3 F110W filter, allowing a more-flexible background model to subtract both galaxies. We modeled the galaxies with a 2D second-order spline, with nodes placed in a grid every $0.076''$ (the natural pixel scale of NICMOS). The WFC3 F110W PSF was modeled as a combination of the elliptical galaxy model and a 2D spline (with a spacing of $0.1''$) using dithered images of a field star. (This is the same empirical PSF model used for testing Tiny-Tim for NICMOS, although there the 2D spline nodes are spaced at the natural pixel scale of NICMOS.) Our testing indicates that this method achieves the same signal-to-noise ratio as the other supernovae that have simpler galaxy subtractions.

- SN SCP06A4: We found a small amount of azimuthal asymmetry in the host. Adding a second-order 2D spline to the galaxy model, with a node spacing of $0.38''$ (five times the natural pixel scale of NICMOS 2) successfully modeled this asymmetry, without adding additional measurement uncertainty to the supernova flux.

- SN SCP05D6: The host galaxy requires two elliptical components to be fitted well. These components are forced to have the same centroid, but are allowed different orientations, ellipticities, and radial profiles. One component forms a bulge, while the other one forms a disk. In one epoch contaminated by the SAA, aperture photometry with a one-pixel radius aperture on the galaxy-model-subtracted images gave better signal-to-noise than PSF photometry, so we used this instead.

- SN SCP06U4: This supernova was on the core of a galaxy that appears to be merging with another galaxy. Similarly to SN SCP05D6, a second elliptical component was needed to model the host, (in this case, a third, detached component was used to model the fainter companion). Our simulated supernovae revealed that, rather than using one host galaxy model to extract photometry, even more precise results were obtained averaging photometry results derived using the elliptical model and the 2D spline model (discussed above for SN SCP06C0). Using this procedure results in a change in flux well inside the error bar.

- SN SCP06H5: The one NICMOS observation of this supernova was our most challenging extraction. The observation of the supernova was 11 rest-frame days after maximum, and it is only $\sim 0.1''$ from the core. As with SN SCP05D6, the host galaxy requires two elliptical components to be fitted well.(Comparing to the 2D spline model discussed above, we obtain photometry that is the same to within a small fraction of the error bar.)

The signal-to-noise ratio of this measurement is low, likely implying some amount of bias due to centroiding error. However, this is the only measurement with a signal-to-noise this low, so no correlation is introduced with any other measurement.

3.3. *Keck AO Photometry*

The photometry of $z > 1.2$ SNe has been almost exclusively measured from HST images (Knop et al. 2003; Riess et al. 2004, 2007; Amanullah et al. 2010). At these redshifts, the rest frame B-band is redshifted beyond 9000 Å, and falls in the near-IR (NIR). NIR observations are typically much easier from space, not only because of the higher spatial resolution of HST compared to ground-based seeing-limited systems, but also because of the lower NIR sky noise in space. However, we show here that adaptive optics on large ground-based telescopes can overcome these limitations and allow high-z SNe to be studied from the ground.

We observed the z=1.315 SN SCP05D6 with the Keck Laser Guide Adaptive Optics (LGS AO) system. These observations were made in the H-band (1.6 μm), which corresponds to the rest-frame R-band. The diffraction-limited resolution of the Keck AO images was $\sim 0.05''$, or a factor of three better than the spatial resolution of HST at these wavelengths. The high spatial resolution meant a much better separation of the SN from the galaxy core compared to HST. It also allows greater contrast between the SN and the sky background. We obtain a photometric precision of 0.14 mag at H$\sim$24 mag in a one hour exposure with Keck AO, showing the potential of AO in SN Ia cosmology.

Melbourne et al. (2007) reports the details of the Keck AO photometry, here we briefly summarize the observations. The Keck LGS AO observing runs for the Center for Adaptive Optics Treasury Survey (Melbourne et al. 2005) coincided with the HST Cluster SN Survey program, and we successfully observed SN SCP05D6 at three epochs, before, near and after the lightcurve maximum.

A 14 mag star, $25''$ away was chosen to provide AO tip-tilt correction. The ~ 11 mag sodium LGS was pointed at the galaxy to provide higher-order AO corrections. The observations were sampled with a $0.01''$ pixel-scale, allowing the diffraction-limited Keck PSF to be fully resolved. Individual exposures of 60s were taken with five dithered pattern positions. The sequence was repeated until sufficient depth was reached. Total exposure times varied from 30 min to 1 hour per epoch.

We were also fortunate to have a 17.9 magnitude natural PSF star only $4''$ away from SN SCP05D6, so the PSF near the location of the SN was well-determined. From the star, we measured a FWHM of $0.055''$ while we had a mean H-band seeing of $0.4''$. Using the observed PSF, the host galaxy was modeled by GALFIT (Peng et al. 2002) and subtracted from the image, providing a clean measurement of the SN diffraction-limited core. Relative photometry with respect to the nearby PSF star was performed at each epoch, and calibrated by the UKIRT standard star FS6 (the photometry is reported in Table 2). The photometric uncertainty was estimated by simulations of model PSFs embedded into the AO image at the same galacto-centric radius as the actual SN.

We fit the SN-lightcurve with the photometric data from

HST/ACS F775W, F850LP, HST/NICMOS F110W, and this Keck/AO observation. We found that the Keck AO data was consistent with the HST observations (Figure 2). Although the uncertainty in the AO measurement was larger than that of HST, including it reduces the color uncertainty by more than 10%, and reduces the sensitivity of the fit to the NICMOS zeropoint uncertainty by more than a third.

4. AUGMENTING THE UNION2 SUPERNOVA COMPILATION: UNION2.1

SNe Ia are an excellent probe of dark energy, as they measure the magnitude-redshift relation with very good precision over a wide range of redshifts, from $z = 0$ up to $z \sim 1.5$ and possibly beyond. While some individual sets of SNe Ia are now, by themselves, large enough to provide constraints on some cosmological parameters (Guy et al. 2010; Kessler et al. 2009), they do not yet constrain the properties of dark energy as well as analyses that combine individual data-sets to create a compilation of SNe Ia that covers a broader range of redshifts. In Kowalski et al. (2008), we developed a systematic methodology for combining the many available datasets into one compilation, called the "Union" compilation.

There are many positive features behind the philosophy adopted by the Union analysis. It includes all SN Ia data-sets on an equal footing, with the same lightcurve fitting, cuts, and outlier rejection. Estimates of the systematic error are entered into a covariance matrix, which can be used for fitting any cosmological model. Choices about how to do the analysis and what cuts to apply are done with the cosmological results hidden. This type of "blind" analysis mitigates biases that arise from inadvertently scrutinizing some data more than others. In Amanullah et al. (2010), we adopted this strategy to create the Union2 compilation. This paper also revised and improved the Union analysis in several significant ways. Firstly, it augmented the Union sample with new SN Ia data-sets from the literature, including 102 low-redshift SNe Ia from the CfA3 survey (Hicken et al. 2009a), 129 intermediate-redshift SNe Ia from the SDSS SN survey (Holtzman et al. 2008), five intermediate-redshift SNe Ia discovered from La Palma (Amanullah et al. 2008), and six new high-redshift SNe Ia. The paper revised the analysis by replacing the SALT lightcurve fitter with SALT2 (Guy et al. 2005, 2007), and handled many systematic errors on a supernova-by-supernova basis in a covariance matrix.

In the current paper, we use the analysis procedure that was used for the Union2 compilation with only one significant change: a correction for the host-mass SN Ia-luminosity relation, described below. The HST calibration and the associated errors have also been updated, as described in Section 4.4.1. We refer to this new compilation as "Union2.1."

4.1. Host Mass Correction to SN Ia Luminosities

There is evidence that SN Ia luminosity correlates with the mass of the host galaxy, even after the corrections for color and light curve width have been applied (Kelly et al. 2010; Sullivan et al. 2010; Lampeitl et al. 2010). Since low-redshift SNe Ia are predominantly from surveys that target catalogued galaxies, the host galaxies of SNe Ia in these surveys are, on average, more massive than the host galaxies of distant SNe Ia from untargeted surveys. SNe Ia from low-redshift samples therefore have brighter absolute magnitudes. Left uncorrected, the correlation biases cosmological results (Sullivan et al. 2010).

Sullivan et al. (2010) find that the correlation can be corrected by fitting a step in absolute magnitude at $m_\star^{\mathrm{threshold}} = 10^{10} m_\odot$. There are two complications with making this correction: most of the SNe in the Union2 compilation do not have host mass data available in the literature, and SN Ia hosts with masses close to the cutoff may scatter across, decreasing the fitted size of the step. To address these problems, we adopt a probabilistic approach to determining the proper host mass correction to apply to each supernova, correcting each supernova by the probability that it belongs in the low-host-mass category. (The low-host-mass category was chosen because most of the low-redshift supernovae are from high-mass galaxies, so correcting the low-host-mass supernovae minimizes the correlation between M_B and the correction coefficient.)

Suppose we have a mass measurement $m_\star^{\mathrm{obs}}$ and we would like to estimate the probability that the true mass $m_\star^{\mathrm{true}}$ is less than the mass threshold. We begin by noting that

$$P(m_\star^{\mathrm{obs}}, m_\star^{\mathrm{true}}) = \qquad (1)$$
$$P(m_\star^{\mathrm{obs}}|m_\star^{\mathrm{true}})P(m_\star^{\mathrm{true}}) \, .$$

We can then integrate this probability over all true host masses less than the threshold:

$$P(m_\star^{\mathrm{true}} < m_\star^{\mathrm{threshold}}|m_\star^{\mathrm{obs}}) = \qquad (2)$$
$$\int_{m_\star^{\mathrm{true}}=0}^{m_\star^{\mathrm{threshold}}} P(m_\star^{\mathrm{obs}}|m_\star^{\mathrm{true}})P(m_\star^{\mathrm{true}})$$

up to a normalization constant found by requiring the integral to be unity when integrating over all possible true masses. $P(m_\star^{\mathrm{true}})$ is estimated from the observed distribution for each type of survey. The SNLS (Sullivan et al. 2010) and SDSS (Lampeitl et al. 2010) host masses were assumed to be representative of untargeted surveys, while the mass distribution in Kelly et al. (2010) was assumed typical of nearby targeted surveys. As these distributions are approximately log-normal, we use this model for $P(m_\star^{\mathrm{true}})$ using the mean and RMS from the log of the host masses from these surveys (with the average measurement errors subtracted in quadrature), giving $\log_{10} P(m_\star^{\mathrm{true}}) = \mathcal{N}(\mu = 9.88, \sigma^2 = 0.92^2)$ for untargeted surveys and $\log_{10} P(m_\star^{\mathrm{true}}) = \mathcal{N}(10.75, 0.66^2)$ for targeted surveys. When host mass measurements are available, $P(m_\star^{\mathrm{obs}}|m_\star^{\mathrm{true}})$ is also modeled as a log-normal; when no measurement is available, a flat distribution is used.

For a supernova from an untargeted survey with no host mass measurement (including supernovae presented in this paper which are not in a cluster), $P(m_\star^{\mathrm{true}} < m_\star^{\mathrm{threshold}})$ is the integral of $P(m_\star^{\mathrm{true}})$ up to the threshold mass: 0.55. Similarly, nearby supernovae from targeted surveys without host galaxy mass measurements are given a $P(m_\star^{\mathrm{true}} < m_\star^{\mathrm{threshold}})$ of 0.13. (Very similar numbers of 0.50 and 0.09 are derived from the observed distribution, without using the log-normal approximation.) We must make the correction for supernovae in clusters, as these are from a targeted survey. We take advantage of the simpler SEDs of early-type galaxies to precisely measure these masses[1].

The best-fit mass-correction coefficient, δ, is much smaller in magnitude (-0.03) than that found in other studies ($\approx$

---

[1] C-001 and F-012 are in clusters, but are not hosted by early-type hosts. We use the untargeted value for their host-mass–luminosity relation correction.

−0.08). This may be due to the small value for δ from the first-year SNLS data, as shown in Table 6. We include the difference in δs as a systematic, as discussed in §4.5. For this analysis, we assumed the host-mass correction does not evolve with redshift.

4.2. *Light-Curve Fitting*

Following Amanullah et al. (2010), we use SALT2 (Guy et al. 2007) to fit supernova lightcurves. The SALT2 model fits three parameters to each SNe: an overall normalization, x_0, to the time dependent spectral energy distribution (SED) of a SN Ia, the deviation, x_1, from the average lightcurve shape, and the deviation, c, from the mean SN Ia $B - V$ color. The three parameters, x_1, c, and integrated B-band flux of the model SALT2 SED at maximum light, $m_B^{\max}$, are then combined with the host mass to form the distance modulus

$$\mu_B = m_B^{\max} + \alpha \cdot x_1 - \beta \cdot c + \delta \cdot P(m_\star^{\mathrm{true}} < m_\star^{\mathrm{threshold}}) - M_B, \tag{3}$$

where M_B is the absolute B-band magnitude of a SN Ia with $x_1 = 0$, $c = 0$ and $P(m_\star^{\mathrm{true}} < m_\star^{\mathrm{threshold}}) = 0$. The parameters α, β, δ and M_B are nuisance parameters that are fitted simultaneously with the cosmological parameters. The SN Ia photometry data and SALT2 light curve fits are shown in Figure 2. The fitted SALT2 parameters are listed in Table 3 as well as the host galaxy host stellar mass and lensing magnification factor.

4.3. *Union2.1*

To the Union2 SN Ia compilation (Amanullah et al. 2010), we add 16 SNe Ia from this paper that were classified as either secure or probable, including six SNe Ia hosted by high-z cluster elliptical galaxies. The four SNe Ia that were classified as possible are not used. We also add 18 SNe Ia from the low-redshift sample of Contreras et al. (2010), 9 of which were not in Union2 (the others had published data from CfA). As in Union2, for all SNe we require

1. that the CMB-centric redshift is greater than 0.015;

2. that there is at least one point between −15 and 6 rest-frame days from B-band maximum light;

3. that there are at least five valid data points;

4. that the entire 68% confidence interval for x_1 lies between −5 and +5;

5. data from at least two bands with rest-frame central wavelength coverage between 2900 Å and 7000 Å; and

6. at least one band redder than rest-frame U-band (4000 Å). This cut is new to this analysis, but only affects SN 2002fx, a GOODS supernova which is very poorly measured.

In addition to these quality cuts, we removed any supernova spectroscopically classified as SN 1991bg-like. These SNe Ia are a distinct subclass which is not modeled well by SALT2. At high redshift, where spectroscopic sub-typing may not be possible, we screen for these supernovae photometrically by searching for any supernovae with red ($c > 0.2$) and narrow-width ($x_1 < -3$) lightcurves, but do not find any. When

fit with SALT2, and color-corrected and shape-corrected (as though they were normal SNe Ia), spectroscopically identified members of this class have an average absolute magnitude only 0.2 magnitudes fainter than normal SNe Ia; any contamination from the handful of supernovae near this cut will have only a small impact (and one well-accounted for by our contamination systematic, see Amanullah et al. (2010)).

From the 16 SNe Ia that were classified as either secure or probable (see Table 1), SN SCP06U4 and SN SCP06K18 fail to pass these cuts. SN SCP06K18 lacks good enough light-curve coverage and SN SCP06U4 fails the x_1 cut[1]. This leaves 14 SNe Ia that are used to constrain the cosmology.

4.4. *Fitting the Cosmology*

Following Amanullah et al. (2010), the best-fit cosmology is determined by minimizing

$$\chi_{\mathrm{stat}}^2 = \sum_{\mathrm{SNe}} \frac{[\mu_B(\alpha, \beta, \delta, M_B) - \mu(z; \Omega_m, \Omega_w, w)]^2}{\sigma_{\mathrm{lc}}^2 + \sigma_{\mathrm{ext}}^2 + \sigma_{\mathrm{sample}}^2}. \tag{4}$$

A detailed discussion of the terms in this equation can be found in Amanullah et al. (2010). We only comment on the final term in the denominator, $\sigma_{\mathrm{sample}}^2$, which is computed by setting the reduced χ^2 of each sample to unity. This term was referred to as "$\sigma_{\mathrm{systematic}}^2$" in Kowalski et al. (2008); Amanullah et al. (2010). We note that $\sigma_{\mathrm{sample}}^2$ includes intrinsic dispersion as well as sample-dependent effects. This term effectively further deweights samples with poorer-quality data that has sources of error which have not been accounted for. As noted in Amanullah et al. (2010), this may occasionally deweight an otherwise well-measured supernova.

Following Conley et al. (2006), Kowalski et al. (2008) and Amanullah et al. (2010), we hide our cosmology results until the full analysis approach is settled. As in previous Union analysis, we carry out an iterative χ^2 minimization with outlier rejection. Each sample is fit for a flat ΛCDM cosmology independently of the other samples (but with α, β, and δ set to their global values). An M_B is chosen for each sample by minimizing the absolute variance-weighted sum of deviations, minimizing the effects of outliers. We then reject any supernova more than 3σ from this fit. All of the SNe Ia in our new sample pass the outlier rejection. As each sample is fit independently with its own Hubble line, systematic errors and the choice of cosmological model are not relevant in this selection.

4.4.1. *Diagnostics*

A diagnostic plot, which is used to study possible inconsistencies between SN Ia samples, is shown in Figure 3. The median of σ_{sample} can be used as a measure of the intrinsic dispersion associated with all SNe Ia. The intrinsic dispersion is a reflection of how well our empirical models correct for the observed dispersion in supernova luminosities. The median σ_{sample} for this paper is 0.15 mag and is indicated with the leftmost dashed vertical line in the left panel.

The variance weighted RMS about the best-fit cosmology gives an indication of the quality of the photometry. A sample with more accurate photometry will have a smaller RMS. For

---

[1] Using an updated version (2-18-17) of SALT2 (or using SALT1), SN SCP06U4 would pass this cut, so this supernova may be included in future analyses.
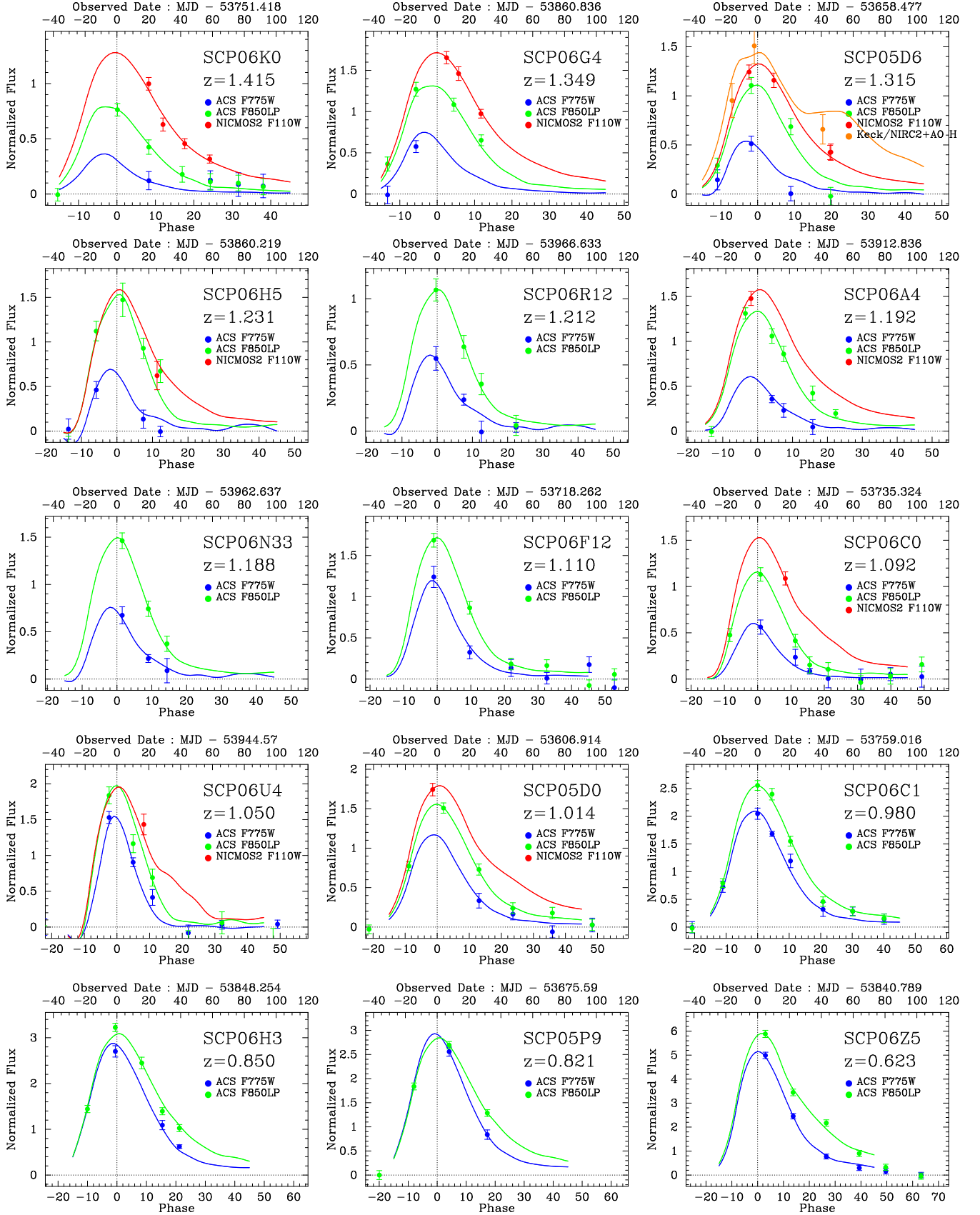
Figure 2. 15 SNe Ia light curve fits by SALT2. Flux is normalized to the z_{850}-band zeropoint magnitude. ACS i_{775}, ACS z_{850} and NICMOS F110W data is color coded in blue, green and red respectively. Note that SCP 05D06 (z=1.314) has H-band data from Keck AO system (orange) (Melbourne et al. 2007) and that this data is consistent with the HST/ACS and HST/NICMOS light curve data.

Table 3
SALT2 Lightcurve Fit Results

SN name	z	MJD_{Bmax}	m_B	x_1	c	Galaxy Mass[a] $(10^{11}M_\odot)$	Lens Factor[b]
SCP06A4	1.192	53912.7 ± 1.5	25.497 ± 0.048	-1.45 ± 0.68	0.065 ± 0.084	0.44	$\cdots$
SCP06C0	1.092	53735.4 ± 1.0	25.636 ± 0.066	-2.66 ± 0.65	0.257 ± 0.083	1.97	$1.030^{+0.007}_{-0.005}$
SCP06C1	0.980	53759.0 ± 0.7	24.613 ± 0.028	-0.35 ± 0.33	0.014 ± 0.053	$\cdots$	$\cdots$
SCP06F12	1.110	53718.4 ± 2.3	25.253 ± 0.068	-2.09 ± 1.29	-0.133 ± 0.142	$\cdots$	$\cdots$
SCP06G4	1.350	53860.9 ± 1.4	25.424 ± 0.052	0.15 ± 0.64	-0.029 ± 0.052	1.72	$1.015^{+0.005}_{-0.004}$
SCP06H3	0.850	53848.2 ± 0.6	24.345 ± 0.038	0.58 ± 0.31	0.089 ± 0.067	$\cdots$	$\cdots$
SCP06H5	1.231	53860.2 ± 1.5	25.389 ± 0.111	-3.12 ± 1.10	-0.103 ± 0.187	3.66	$\cdots$
SCP06K0	1.415	53751.3 ± 2.8	25.811 ± 0.087	0.30 ± 0.97	0.147 ± 0.081	2.30	$\cdots$
SCP06N33	1.188	53962.6 ± 4.3	25.407 ± 0.132	-2.15 ± 1.32	-0.038 ± 0.175	$\cdots$	$1.066^{+0.017}_{-0.014}$
SCP05D0	1.014	53606.9 ± 0.9	25.201 ± 0.066	-0.61 ± 0.65	0.061 ± 0.085	0.40	$\cdots$
SCP05D6	1.315	53658.5 ± 1.3	25.660 ± 0.046	-1.26 ± 0.56	-0.058 ± 0.061	2.61	$1.021^{+0.012}_{-0.008}$
SCP05P9	0.821	53675.6 ± 0.6	24.367 ± 0.049	0.25 ± 0.50	0.022 ± 0.075	$\cdots$	$\cdots$
SCP06R12	1.212	53966.6 ± 3.5	25.789 ± 0.114	-2.06 ± 1.50	-0.158 ± 0.198	0.23	$\cdots$
SCP06U4	1.050	53944.4 ± 1.1	25.056 ± 0.063	-4.62 ± 1.09	-0.102 ± 0.096	1.11	$\cdots$
SCP06Z5	0.623	53840.5 ± 3.0	23.482 ± 0.144	-0.76 ± 0.88	0.070 ± 0.120	$\cdots$	$\cdots$

[a] The details of host galaxy identifications, coordinates and its stellar mass measurements can be found in Meyers et al. (2011).
[b] Gravitational lensing magnification factor (see §2.1 for details). For cosmological analysis we must divide the corrected SNe fluxes by this factor to make use of these supernovae.
[c] SCP06U4 is not included in our current cosmological results, but will likely be included in future compilations (see §4 for details).
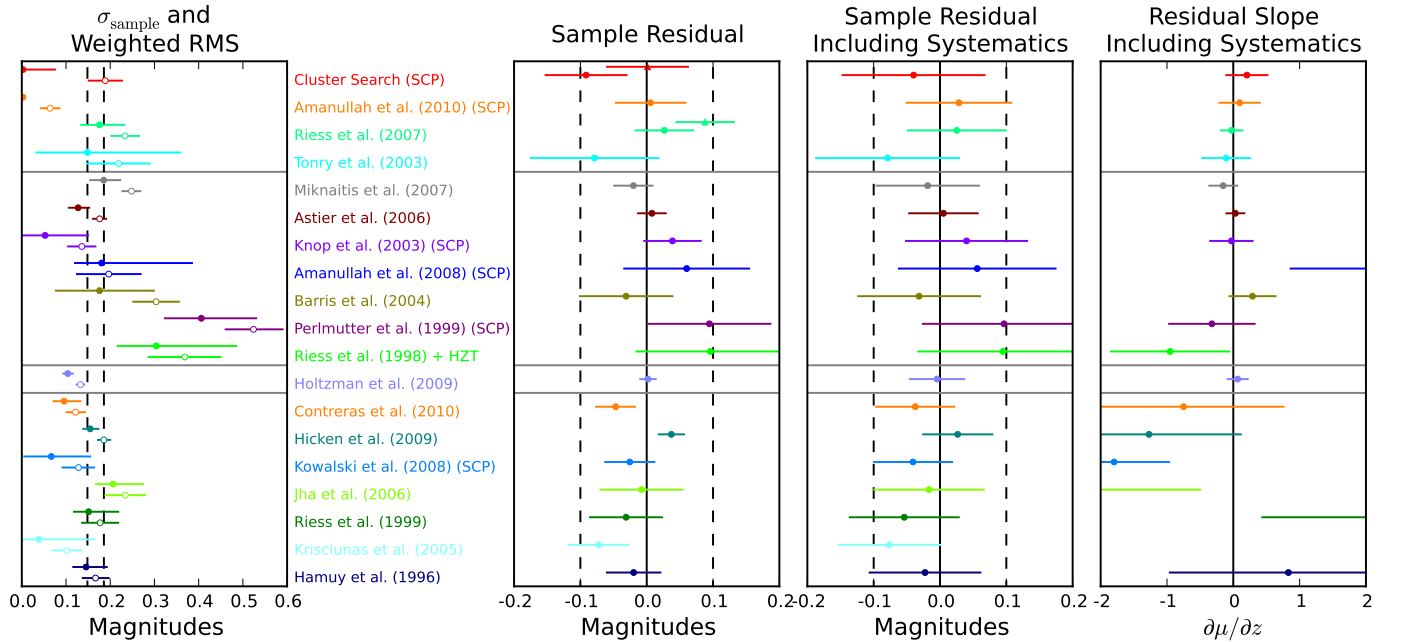

Figure 3. Diagnostics plot for the individual data sets. From left to right: irreducible sample dispersion (filled circles) and variance-weighted RMS about the best-fit model (open circles); the average sample residual from the best-fit model ($\mu_{measured} - \mu_{model}$) excluding and including systematic errors; and the best-fit slope of the Hubble residual (in magnitudes) versus redshift — $\partial\mu_{residual}/\partial z$. Note that the errors on the sample dispersion include only statistical errors and do not include possible systematic errors. The confidence intervals on the weighed RMS are obtained with Monte-Carlo simulations. The triangles in the sample residual plot show the effect of including the filter shifts discussed in Section 4.4.1.

SNe Ia from our survey, the RMS is 0.19 ± 0.04, which is only slightly larger than that measured for the 1st year SN Ia sample from SNLS, and equal to the median of all samples (shown as the rightmost dashed line in Figure 3, left panel).

The two middle panels show the tension between data-sets, the first with statistical errors only, and the second with statistical and systematic errors (see §4.5). Most samples land within 1 σ of the mean defined by all samples and about one third lie outside 1 σ, as expected for a normal distribution. No sample exceeds 2 σ. The right hand panel shows the slope of the residuals, which, for larger data sets, can be used to reveal Malmquist-like biases or calibration errors.

The supernovae from our sample are 1.5-σ brighter than the average sample. While the source of the difference may certainly be a simple statistical fluctuation, part of the difference might be attributable to errors in the filter responses of the ACS filters. (The difference is largely driven by the SNe Ia that have only ACS i_{775} and z_{850} data to constrain their light curves.) Based on photometric observations of spectrophotometric standards, Bohlin (2007) report possible blueward shifts of 94 Å for the z_{850} filter and 57 Å for the i_{775} filter (with smaller shifts in bluer filters). The red triangle in the sample residual panel shows the effect of applying these shifts. The shifts also affect the GOODS supernovae. The green triangle shows the affect of applying the filter shifts to those data. Bohlin (2007) notes that more data to confirm the filter shifts are needed, so we do not apply them in our primary analysis. Instead, we include the uncertainty in the filter curves as a systematic error, as described in §4.5.

Part of the difference could also be due to the correction that we apply for the recently discovered correlation between host galaxy mass and the luminosity of SNe Ia after the lightcurve width and color corrections have been applied. Many of the hosts in our sample are massive early type galaxies. In this analysis, the correction we use is smaller than the correction that has been noted by others. We add this difference as a systematic error, as described in §4.5.

Figure 4 shows the Hubble Diagram with SNe from the updated Union2 sample and the best-fit ΛCDM model. We add 14 SNe Ia from this current paper. (As discussed above, SN SCP06U4 is likely to be included in future analyses so it is included on the plot with a different symbol.) Ten (eleven with SN SCP06U4) are above a redshift of one, significantly increasing the number of well-measured supernovae above this redshift.

4.5. Systematic errors

In this paper, we follow the systematics analysis we presented in Amanullah et al. (2010). Systematic errors that directly affect supernova distance measurements (calibration, and galactic extinction, for example) are treated as nuisance parameters to be fit simultaneously with the cosmology. Minimizing over these nuisance parameters gives additional terms to add to the distance modulus covariance matrix

$$U_{ij} = \sum_{\epsilon} \frac{d\mu_i(\alpha,\beta)}{d\epsilon} \frac{d\mu_j(\alpha,\beta)}{d\epsilon} \sigma_\epsilon^2 , \qquad (5)$$

where the sum is over each of these distance systematic errors in the analysis. (Although the distance modulus depends on δ as well as α and β, the derivatives with respect to the zero-points do not.) In this analysis, α and β have little interaction with cosmological parameters. When computing cosmological constraints, we therefore freeze the covariance matrix in

order to avoid multiple matrix inversions[1]. Only when the α and β may vary significantly from the global best-fit (Table 6), do we update α and β.

Systematic errors that affect sample composition or the color and shape correction coefficients cannot be parameterized supernova-by-supernova in this way. These are incorporated by assigning each dataset its own constant covariance. This is an adequate treatment, as these systematic errors are subdominant.

There are two systematic errors that were not included in Amanullah et al. (2010), but are included in this analysis for the first time: a systematic error on the host-mass correction coefficient, δ (which might affect δ at the ~ 0.05 level), and uncertainties in the effective wavelengths of the ACS i_{775} and z_{850} filters.

In addition to updating the NICMOS F110W zeropoint and uncertainty, as described in §3.2.1, we revise the uncertainty assigned to the zeropoint for NICMOS F160W to account for the uncertainty in the count-rate non-linearity at this wavelength (de Jong et al. 2006). Table 4 gives the assumed zeropoint error for each filter.

We note that the nearby supernovae from targeted searches are sensitive to δ (relative to the untargeted searches) at the level of $(0.55 - 0.13)\Delta\delta \approx 0.02$ magnitudes, while the covariance weighted mean of the cluster supernovae varies with δ as $0.24\Delta\delta \approx 0.01$ magnitudes. We cannot propagate this systematic on a supernova-by-supernova basis, as this would be equivalent to fitting for δ, which we already do. Therefore, we include this error by adding a covariance of 0.02^2 to the nearby, targeted supernova surveys, a covariance of 0.01^2 to our new data-set, and $0.02 \cdot 0.01$ between these data-sets.

Including uncertainties in filter effective wavelength is not as straightforward as including zeropoint uncertainties. Effective wavelength is only the first-order method of describing a filter. For a simple filter shift, as implemented here, $d\mu(\alpha,\beta)/d\lambda$ will undergo significant variations as supernova spectral features shift in and out of the filter. These are likely to be worse than the actual effect of simply reweighting filter throughput. Although in general these variations will get averaged out with different phases, redshifts, and additional filters, we have modeled a worst-case in accounting for this systematic (and even then it only affects the supernovae most dependent on z_{850}).

Table 5 shows the impact of each type of systematic error on our cosmological constraints, in combination with BAO, CMB, and H_0 data (see §5). For the purpose of constructing Table 5, we add, for each systematic error in the table, the contribution from just that systematic to the statistical-only covariance matrix. The confidence interval for constant w where the χ^2 is within 1 of the minimum χ^2 (the edges of this confidence interval are hereafter referred to with the notation $\Delta\chi^2 = 1$) is found iteratively; the plus and minus errors for constant w are averaged. The statistical-only constant w error bar is subtracted in quadrature, leaving the effect of each systematic on constant w. We also quote the effect of each systematic error of the $\Delta\chi^2 = 5.99$ confidence contour in the (w_0, w_a) plane; as this is two-dimensional, we subtract the area (not in quadrature) of the statistical-only contour.

Since the derived cosmology errors vary with the best-fit cosmology, after a given systematic error has been added, the

---

[1] As demonstrated in the Union2 appendix, these matrix inversions can be simplified at the expense of more matrix multiplication; the run-time does not change much.
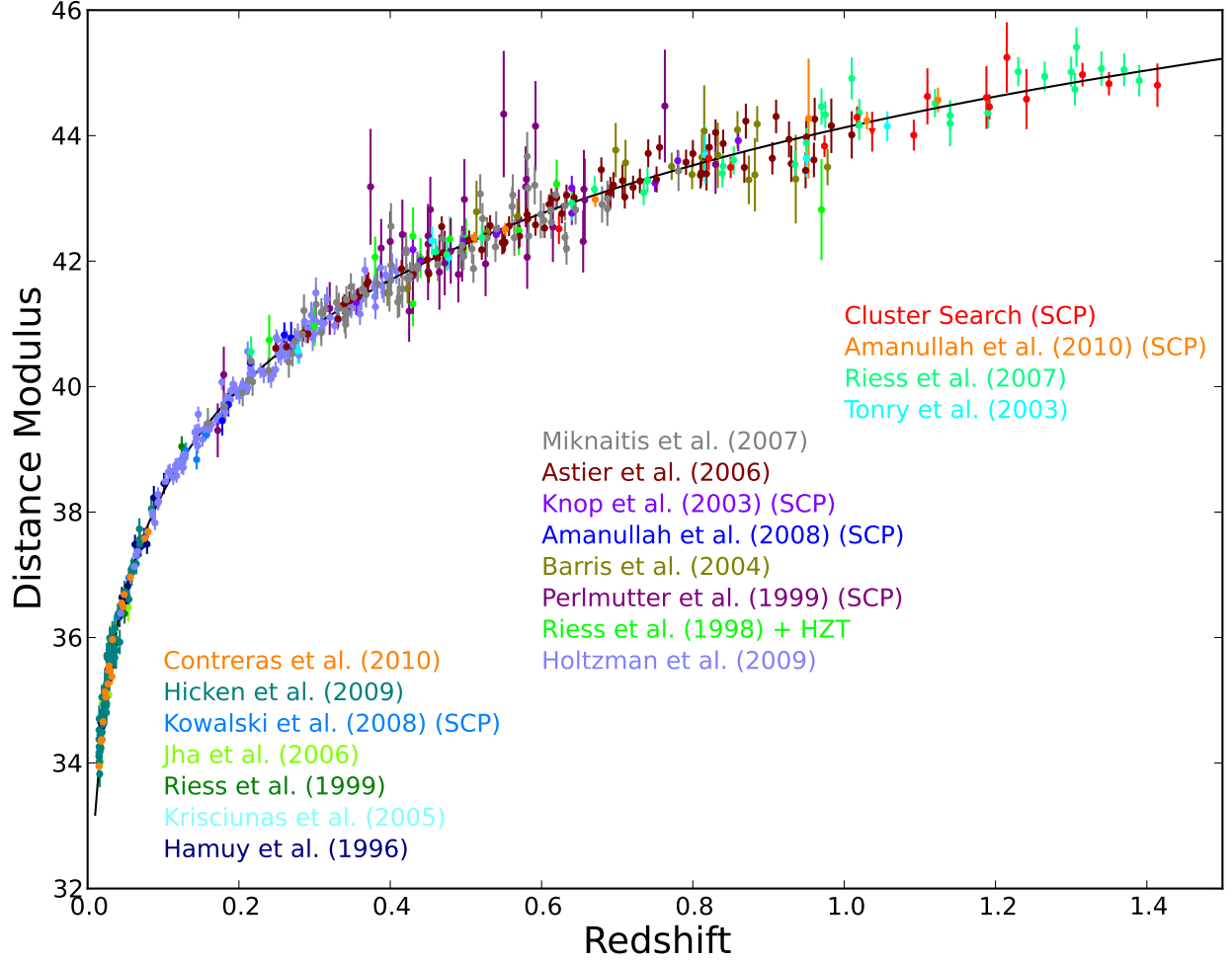
Figure 4. Hubble diagram for the Union2.1 compilation. The solid line represents the best-fit cosmology for a flat ΛCDM Universe for supernovae alone. SN SCP06U4 falls outside the allowed x_1 range and is excluded from the current analysis. When fit with a newer version of SALT2, this supernova passes the cut and would be included, so we plot it on the Hubble diagram, but with a red triangle symbol.

Table 4
Assumed instrumental uncertainties for SNe in this paper.

Source	Band	Uncertainty	Reference
HST	WFPC2	0.02	Heyer et al. (2004)
	ACS F850LP	0.01	Bohlin (2007)
	ACS F775W	0.01	
	ACS F606W	0.01	
	ACS F850LP	94 Å	Bohlin (2007)
	ACS F775W	57 Å	
	ACS F606W	27 Å	
	NICMOS J	0.024	Ripoche et. al. (in prep), Section 3.2.1
	NICMOS H	0.06	de Jong et al. (2006)
SNLS	g, r, i	0.01	Astier et al. (2006)
	z	0.03	
ESSENCE	R, I	0.014	Wood-Vasey et al. (2007)
SDSS	u	0.014	Kessler et al. (2009)
	g, r, i	0.009	
	z	0.010	
SCP: Amanullah et al. (2010)	R, I	0.03	Amanullah et al. (2010)
	J	0.02	
Other	U-band	0.04	Hicken et al. (2009a)
	Other Band	0.02	Hicken et al. (2009a)

Table 5
Effect on constant w error bars and area of the 95% $w_0 - w_a$ confidence contour (inverse DETF FoM) for each type of systematic error, when SN Ia constraints are combined with constraints from CMB, H$_0$, and BAO.

Source	Error on Constant w	Inverse DETF FoM
Vega	0.033	0.19
All Instrument Calibration	0.030	0.18
(ACS Zeropoints)	0.003	0.01
(ACS Filter Shift)	0.007	0.04
(NICMOS Zeropoints)	0.007	¡0.01
Malmquist Bias	0.020	0.07
Color Correction	0.020	0.07
Mass Correction	0.016	0.08
Contamination	0.016	0.05
Intergalactic Extinction	0.013	0.03
Galactic Extinction Normalization	0.010	0.01
Rest-Frame U-Band Calibration	0.009	¡0.01
Lightcurve Shape	0.006	¡0.01
Quadrature Sum of Errors/ Sum of Area (not used)	*0.061*	*0.68*
Summed in Covariance Matrix	0.048	0.42

supernova magnitudes are shifted so that the best-fit cosmology including that systematic matches the best-fit with statistical errors only. This magnitude adjustment (which is the same adjustment we use for blinding ourselves to the best-fit cosmology) consists of repeatedly computing the difference in distance modulus between the best-fit cosmology and fiducial value and adding it to the supernovae.

As with the Union2 compilation, calibration systematics represent the largest contribution to the error on constant w. Here, we see that they are also the dominant systematics for (w_0, w_a). As noted by Amanullah et al. (2010), significantly smaller systematic errors are derived by adding each covariance in the covariance matrix, rather than adding the cosmological impacts together. This is due to the different redshift dependence of each systematic error, as well as some self-calibration that occurs as described in Amanullah et al. (2010).

Some potential systematic errors can be investigated by dividing the whole dataset into subsets. Table 6 shows many of these divisions. All of the numbers are computed including supernova systematics; the cosmological constraints are computed including BAO and CMB data. In short, we do not see any evidence of unknown systematic errors, requiring the cosmological impact to be smaller than the current errors.

The first subsets are subsets in redshift. These can be used to study possible evolution of correction coefficients for shape, color, and host mass. The redshift range 0.5 to 1 seems to show β and δ smaller in magnitude, but the revised SNLS sample (Guy et al. 2010) which uses a newer version of the calibration and lightcurve fitting (as well as many more supernovae), shows no signs of this. As we have already budgeted these systematic uncertainties, these updates will be within our error bars.

The next rows show the effect of changing δ from 0 to -0.08 (the size of the correction in Sullivan et al. (2010)). Because a large error on δ is already included in the systematic error covariance matrix, this has less than a 0.01 effect on w, about ten times smaller than it would have if we did not include this systematic.

Next, we consider systematics caused by potentially different populations of supernovae. We perform a cut on the best-fit true x_1 or c of each supernova (see Amanullah et al. (2010) for details). The cosmology in each case is compatible with the cosmology derived from the whole sample.

We now look at each of the four largest datasets for evidence of tension. The only tension found is in the first-year SNLS sample (Astier et al. 2006). Here, β and δ are both at odds with the whole sample, but as noted above, we do not believe this is a cause for concern.

The final two rows show the high-redshift sample split by host type; this is discussed in §6.2.

5. CONSTRAINTS ON DARK ENERGY

Following Amanullah et al. (2010), we constrain the properties of dark energy first using SNe Ia alone (with and without systematics), and then by combining the constraints derived from SNe Ia with those derived from the 7-year WMAP data of the CMB (Komatsu et al. 2011), the position of the BAO peak from the combined analysis of the SDSS DR7 and 2dFGRS data (Percival et al. 2010), and the measurement of the Hubble constant (H_0) from Cepheids (Riess et al. 2011).

The rate of expansion at redshift z, $H(z)$, is described by the Friedman equation:

$$\frac{H^2(z)}{H_0^2} = \Omega_m(1+z)^3 + \Omega_k(1+z)^2 \qquad (6)$$
$$+ \Omega_{\rm DE} \exp\left[\int 3(1+w(z)){\rm dln}(1+z)\right],$$

where H_0 is the rate of expansion today, Ω_m and $\Omega_{\rm DE}$ are the matter and dark energy density with respect to the critical density today, $w(z)$, is the dark energy equation-of-state parameter, and $\Omega_k = 1 - \Omega_m - \Omega_{\rm DE}$ is the spatial curvature density of the universe. Distances, such as the luminosity distance, depend on the integral of $1/H(z)$ over redshift.

In this section, we consider the following models for dark energy:

- ΛCDM: A cosmological constant in a flat universe.

- wCDM: A constant equation-of-state parameter in a flat universe.

- owCDM: A constant equation-of-state parameter in a curved universe.

- w_zCDM models: A time-varying equation-of-state parameter in universes with and without curvature.

The results for each of the models are listed in Table 7 and discussed in turn in the following sub-sections. Unless stated otherwise, the uncertainties represent the 68% confidence limits ($\Delta\chi^2 = 1$) and include both statistical uncertainties and systematic errors.

5.1. ΛCDM

In the ΛCDM model, the equation-of-state parameter is exactly -1 and does not vary with time. In a flat Universe, SNe Ia alone constrain the dark-energy density, Ω_Λ, to be $\Omega_\Lambda = 0.705^{+0.040}_{-0.043}$ including systematics. Adding the constraints from CMB, BAO and H_0 reduces the uncertainty. Under the assumption of a flat Universe, the four probes yield

$$\Omega_\Lambda = 0.729^{+0.014}_{-0.014} \quad (\Lambda{\rm CDM : SN + CMB + BAO + H_0})$$

In this ΛCDM model, the expansion of the universe switched from deceleration to acceleration at $z = 0.752 \pm 0.041$, which corresponds to a look back time of 6.62 ± 0.22 Gyr, about the half of the age of the universe. Equality between the energy density of dark energy and matter occurred later, at $z = 0.391 \pm 0.033$ or the look back time of 4.21 ± 0.27 Gyr.

In Figure 5, we show the confidence intervals on Ω_m and Ω_Λ from SNe, CMB and BAO. Both the individual constraints and the combined constraint are shown (the BAO constraints are computed with an $\Omega_m h^2$ prior from the CMB). The SN constraint is almost orthogonal to that of the CMB. If we remove the flatness prior, the best-fit Ω_m and Ω_Λ change by a fraction of their errors with $\Omega_k = 0.002^{+0.005}_{-0.005}$.

5.2. wCDM : Constant Equation of State with $w \neq -1$

In wCDM models, w is constant but is allowed to be different from -1. While few dark energy theories give $w \neq -1$ and yet constant (Copeland et al. 2006), the constant w model is still useful to constrain as it contains fewer parameters than

Table 6
Constraints on standardization and cosmological parameters for subsets. M_B is the B-band corrected absolute magnitude; α, β, and δ are the lightcurve shape, color, and host mass correction coefficients, respectively. The outlier rejection is redone each time, so the totals may not add up to the whole sample. The constraints are computed including BAO, CMB, and H_0 constraints and supernova systematic errors.

Subset	Number	$M_B(h=0.7)$	α	β	δ	Ω_m	w
Whole Sample							
$z \geq 0.015$	580	$-19.321^{+0.030}_{-0.030}$	$0.121^{+0.007}_{-0.007}$	$2.47^{+0.06}_{-0.06}$	$-0.032^{+0.031}_{-0.031}$	$0.271^{+0.015}_{-0.014}$	$-1.013^{+0.068}_{-0.074}$
Correction Coefficients, Split by Redshift							
$0.015 \leq z \leq 0.10$	175	$-19.328^{+0.037}_{-0.038}$	$0.118^{+0.011}_{-0.011}$	$2.57^{+0.08}_{-0.08}$	$-0.027^{+0.054}_{-0.054}$	0.270 (fixed)	-1.000 (fixed)
$0.100 \leq z \leq 0.25$	75	$-19.371^{+0.054}_{-0.054}$	$0.146^{+0.019}_{-0.019}$	$2.56^{+0.18}_{-0.17}$	$-0.087^{+0.060}_{-0.060}$	0.270 (fixed)	-1.000 (fixed)
$0.250 \leq z \leq 0.50$	152	$-19.317^{+0.046}_{-0.046}$	$0.116^{+0.014}_{-0.013}$	$2.46^{+0.12}_{-0.12}$	$-0.042^{+0.066}_{-0.066}$	0.270 (fixed)	-1.000 (fixed)
$0.500 \leq z \leq 1.00$	137	$-19.307^{+0.048}_{-0.049}$	$0.124^{+0.019}_{-0.019}$	$1.46^{+0.19}_{-0.19}$	$0.023^{+0.060}_{-0.060}$	0.270 (fixed)	-1.000 (fixed)
$z \geq 1.000$	25	$-19.289^{+0.217}_{-0.254}$	$-0.019^{+0.072}_{-0.076}$	$3.48^{+1.13}_{-0.89}$	$-0.151^{+0.384}_{-0.446}$	0.270 (fixed)	-1.000 (fixed)
Effect of δ on w							
$z \geq 0.015$	580	$-19.340^{+0.026}_{-0.026}$	$0.123^{+0.007}_{-0.007}$	$2.47^{+0.06}_{-0.06}$	-0.080 (fixed)	$0.272^{+0.015}_{-0.014}$	$-1.004^{+0.067}_{-0.072}$
$z \geq 0.015$	580	$-19.303^{+0.031}_{-0.031}$	$0.120^{+0.007}_{-0.007}$	$2.47^{+0.06}_{-0.06}$	0.000 (fixed)	$0.271^{+0.015}_{-0.014}$	$-1.013^{+0.069}_{-0.075}$
Cosmological Results, Split by Lightcurve Color and Shape							
$c \geq 0.05$	256	$-19.387^{+0.037}_{-0.038}$	$0.118^{+0.011}_{-0.011}$	$2.77^{+0.09}_{-0.09}$	$-0.057^{+0.052}_{-0.052}$	$0.269^{+0.015}_{-0.014}$	$-1.028^{+0.077}_{-0.084}$
$c \leq 0.05$	321	$-19.323^{+0.030}_{-0.030}$	$0.125^{+0.011}_{-0.010}$	$1.29^{+0.32}_{-0.33}$	$-0.057^{+0.038}_{-0.038}$	$0.275^{+0.015}_{-0.014}$	$-0.982^{+0.069}_{-0.075}$
$x_1 \geq -0.25$	311	$-19.366^{+0.041}_{-0.041}$	$0.020^{+0.026}_{-0.025}$	$2.58^{+0.10}_{-0.10}$	$-0.004^{+0.047}_{-0.047}$	$0.269^{+0.015}_{-0.014}$	$-1.037^{+0.077}_{-0.085}$
$x_1 \leq -0.25$	269	$-19.386^{+0.044}_{-0.045}$	$0.152^{+0.021}_{-0.020}$	$2.43^{+0.08}_{-0.08}$	$-0.087^{+0.050}_{-0.050}$	$0.267^{+0.015}_{-0.014}$	$-1.045^{+0.077}_{-0.084}$
Correction Coefficients and M_B for the Large Datasets							
Hicken et al. (2009)	94	$-19.314^{+0.055}_{-0.055}$	$0.115^{+0.015}_{-0.015}$	$2.74^{+0.11}_{-0.11}$	$-0.053^{+0.098}_{-0.099}$	0.270 (fixed)	-1.000 (fixed)
Holtzman et al. (2009)	129	$-19.336^{+0.051}_{-0.051}$	$0.149^{+0.014}_{-0.013}$	$2.40^{+0.15}_{-0.14}$	$-0.061^{+0.050}_{-0.050}$	0.270 (fixed)	-1.000 (fixed)
Miknaitis et al. (2007)	74	$-19.325^{+0.078}_{-0.080}$	$0.113^{+0.037}_{-0.035}$	$2.49^{+0.17}_{-0.16}$	0.000 (fixed)	0.270 (fixed)	-1.000 (fixed)
Astier et al. (2006)	71	$-19.292^{+0.047}_{-0.048}$	$0.145^{+0.019}_{-0.018}$	$1.70^{+0.18}_{-0.18}$	$-0.023^{+0.040}_{-0.040}$	0.270 (fixed)	-1.000 (fixed)
$z > 0.9$, Split by Galaxy Host							
Early Type $z > 0.9$	13	$-19.388^{+0.139}_{-0.186}$	$0.112^{+0.139}_{-0.151}$	$3.16^{+1.84}_{-1.26}$	0.000 (fixed)	0.270 (fixed)	-1.000 (fixed)
Late Type $z > 0.9$	15	$-19.141^{+0.067}_{-0.067}$	$0.094^{+0.049}_{-0.041}$	$0.49^{+0.85}_{-0.69}$	0.000 (fixed)	0.270 (fixed)	-1.000 (fixed)

the dynamical dark energy models considered in the next section, and a value different from -1 would rule out the cosmological constant.

In a flat universe ($\Omega_k = 0$), SNe Ia alone give $w = -1.001^{+0.348}_{-0.398}$ (including systematics). Adding the constraints from the other three probes tightens the constraint on w considerably, as the constraints from SNe Ia in the $\Omega_m - w$ parameter plane are almost orthogonal to those provided by BAO and the CMB (Figure 6).

In principle, a constraint on H_0 helps to break the degeneracy between Ω_m and h for CMB, which measures $\Omega_m h^2$ (Spergel et al. 2003). However, in this case adding supernova data helps more, as narrowing the degeneracy between Ω_m and w allows the CMB itself to constrain H_0. By combining all four probes, we find $w = -1.013^{+0.068}_{-0.073}$. As seen in Table 7, neither BAO nor H_0 currently make much of a difference in the error bars for this model.

5.3. *owCDM : Constant Equation of State in a Curved Universe*

Inflation models generally predict that the curvature of the Universe, Ω_k, is $\sim 10^{-5}$ (Guth 1981; Liddle & Lyth 2000). In curved universes, SNe Ia play the critical role in constraining w, while CMB+BAO constrain Ω_k and Ω_m. By combining all four probes, we find $\Omega_k = 0.002^{+0.007}_{-0.007}$ and $w = -1.003^{+0.091}_{-0.095}$. Even with the additional freedom for non-zero curvature, a flat universe is supported from observations. Among many cosmological parameters, the curvature of the universe is the most well-determined parameter.

We note CMB alone does not place a tight constraint on curvature[1], $\Omega_k = -0.102^{+0.085}_{-0.097}$ (Komatsu et al. 2011), and it is the combination of SN Ia and BAO which improves the constraint by a factor of ten. Including H_0 improves the curvature constraints but the current measurements from SNe Ia and BAO have more impact.

For the equation-of-state parameter w, as seen in Table 7, BAO constraints are now needed to constrain Ω_m, while H_0 again has a small impact on the w measurement.

5.4. *Time Dependent Equation of State*

We next examine models in which dark energy changes with time. For a wide range of dark energy models, it can be shown (Linder 2003) that, to good approximation, the dark energy equation-of-state can be parametrized by

$$w(a) = w_0 + w_a(1 - a) \qquad (7)$$

[1] http://lambda.gsfc.nasa.gov/product/map/dr4/parameters.cfm

Table 7

Fit results on cosmological parameters Ω_m, w_0, w_a and Ω_k. The parameter values are followed by their statistical (first column) and statistical and systematic (second column) 1σ ($\Delta\chi^2 = 1$) uncertainties. For the fits including curvature and time-varying w, the confidence intervals can be quite non-gaussian and we also show $\Delta\chi^2 = 4$ confidence intervals (with and without systematics) for comparison.

Fit	Ω_m	Ω_m w/ Sys	Ω_k	Ω_k w/ Sys	w_0	w_0 w/ Sys	w_a	w_a w/ Sys
				ΛCDM				
SNe	$0.277^{+0.022}_{-0.021}$	$0.295^{+0.043}_{-0.040}$	0 (fixed)	0 (fixed)	-1 (fixed)	-1 (fixed)	0 (fixed)	0 (fixed)
SNe+BAO+CMB	$0.278^{+0.014}_{-0.013}$	$0.282^{+0.017}_{-0.016}$	0 (fixed)	0 (fixed)	-1 (fixed)	-1 (fixed)	0 (fixed)	0 (fixed)
SNe+BAO+CMB+H_0	$0.271^{+0.012}_{-0.012}$	$0.271^{+0.014}_{-0.014}$	0 (fixed)	0 (fixed)	-1 (fixed)	-1 (fixed)	0 (fixed)	0 (fixed)
				$o\Lambda$CDM				
SNe+BAO+CMB	$0.282^{+0.015}_{-0.014}$	$0.286^{+0.018}_{-0.017}$	$-0.004^{+0.006}_{-0.006}$	$-0.004^{+0.006}_{-0.007}$	-1 (fixed)	-1 (fixed)	0 (fixed)	0 (fixed)
SNe+BAO+CMB+H_0	$0.271^{+0.013}_{-0.012}$	$0.272^{+0.014}_{-0.014}$	$0.002^{+0.005}_{-0.005}$	$0.002^{+0.005}_{-0.005}$	-1 (fixed)	-1 (fixed)	0 (fixed)	0 (fixed)
				wCDM				
SNe	$0.281^{+0.067}_{-0.092}$	$0.296^{+0.102}_{-0.180}$	0 (fixed)	0 (fixed)	$-1.011^{+0.208}_{-0.231}$	$-1.001^{+0.348}_{-0.398}$	0 (fixed)	0 (fixed)
SNe+BAO+H_0	$0.309^{+0.029}_{-0.028}$	$0.320^{+0.035}_{-0.033}$	0 (fixed)	0 (fixed)	$-1.097^{+0.091}_{-0.106}$	$-1.076^{+0.117}_{-0.133}$	0 (fixed)	0 (fixed)
SNe+CMB	$0.271^{+0.018}_{-0.017}$	$0.279^{+0.025}_{-0.023}$	0 (fixed)	0 (fixed)	$-0.983^{+0.051}_{-0.056}$	$-0.955^{+0.075}_{-0.079}$	0 (fixed)	0 (fixed)
SNe+BAO+CMB	$0.278^{+0.014}_{-0.014}$	$0.285^{+0.018}_{-0.017}$	0 (fixed)	0 (fixed)	$-0.993^{+0.052}_{-0.055}$	$-0.951^{+0.075}_{-0.081}$	0 (fixed)	0 (fixed)
SNe+BAO+CMB+H_0	$0.272^{+0.013}_{-0.013}$	$0.271^{+0.014}_{-0.014}$	0 (fixed)	0 (fixed)	$-1.008^{+0.050}_{-0.054}$	$-1.013^{+0.068}_{-0.073}$	0 (fixed)	0 (fixed)
				owCDM				
SNe+CMB	$0.281^{+0.069}_{-0.087}$	$0.295^{+0.109}_{-0.161}$	$-0.003^{+0.034}_{-0.027}$	$-0.005^{+0.067}_{-0.041}$	$-1.007^{+0.179}_{-0.194}$	$-0.993^{+0.299}_{-0.331}$	0 (fixed)	0 (fixed)
SNe+BAO+CMB	$0.283^{+0.016}_{-0.015}$	$0.287^{+0.018}_{-0.017}$	$-0.004^{+0.007}_{-0.007}$	$-0.002^{+0.008}_{-0.008}$	$-1.012^{+0.058}_{-0.062}$	$-0.975^{+0.094}_{-0.098}$	0 (fixed)	0 (fixed)
SNe+BAO+CMB+H_0	$0.272^{+0.013}_{-0.013}$	$0.272^{+0.015}_{-0.014}$	$0.002^{+0.006}_{-0.006}$	$0.002^{+0.007}_{-0.007}$	$-1.006^{+0.056}_{-0.060}$	$-1.003^{+0.091}_{-0.095}$	0 (fixed)	0 (fixed)
				w_zCDM				
SNe+CMB	$0.273^{+0.022}_{-0.020}$	$0.281^{+0.043}_{-0.028}$	0 (fixed)	0 (fixed)	$-1.006^{+0.165}_{-0.182}$	$-0.993^{+0.263}_{-0.307}$	$0.11^{+0.75}_{-0.77}$	$0.17^{+1.08}_{-1.19}$
SNe+BAO+CMB	$0.278^{+0.014}_{-0.014}$	$0.284^{+0.018}_{-0.017}$	0 (fixed)	0 (fixed)	$-1.052^{+0.126}_{-0.120}$	$-1.013^{+0.183}_{-0.173}$	$0.30^{+0.48}_{-0.62}$	$0.26^{+0.57}_{-0.74}$
SNe+BAO+CMB+H_0	$0.271^{+0.013}_{-0.013}$	$0.270^{+0.015}_{-0.014}$	0 (fixed)	0 (fixed)	$-1.021^{+0.123}_{-0.117}$	$-1.046^{+0.179}_{-0.170}$	$0.07^{+0.49}_{-0.60}$	$0.14^{+0.60}_{-0.76}$
				ow_zCDM				
SNe+CMB	$0.177^{+0.086}_{-0.093}$	$0.190^{+0.208}_{-0.154}$	$0.075^{+0.065}_{-0.128}$	$0.073^{+0.115}_{-0.141}$	$-0.988^{+0.176}_{-0.202}$	$-0.969^{+0.284}_{-0.345}$	$0.90^{+0.26}_{-3.88}$	$0.89^{+0.43}_{-5.25}$
SNe+BAO+CMB	$0.283^{+0.019}_{-0.017}$	$0.286^{+0.022}_{-0.023}$	$-0.004^{+0.017}_{-0.010}$	$-0.001^{+0.037}_{-0.013}$	$-1.010^{+0.169}_{-0.178}$	$-0.997^{+0.266}_{-0.293}$	$-0.01^{+1.04}_{-1.05}$	$0.13^{+1.16}_{-1.57}$
SNe+BAO+CMB+H_0	$0.270^{+0.014}_{-0.013}$	$0.274^{+0.016}_{-0.015}$	$0.025^{+0.008}_{-0.008}$	$0.027^{+0.012}_{-0.011}$	$-1.218^{+0.069}_{-0.072}$	$-1.198^{+0.100}_{-0.112}$	$1.21^{+0.10}_{-1.14}$	$1.19^{+0.13}_{-0.13}$
SNe+BAO+CMB+H_0 ($\Delta\chi^2 = 4.0$)	$0.270^{+0.029}_{-0.026}$	$0.274^{+0.032}_{-0.029}$	$0.025^{+0.016}_{-0.035}$	$0.027^{+0.026}_{-0.036}$	$-1.218^{+0.425}_{-0.147}$	$-1.198^{+0.293}_{-0.227}$	$1.21^{+0.19}_{-2.49}$	$1.19^{+0.27}_{-2.40}$

where $a = 1/(1 + z)$ is a scale factor. The ΛCDM model is recovered when $w_0 = -1$ and $w_a = 0$. The constraints on w_0 and w_a are shown in Figure 7 and Table 7.

The Dark Energy Task Force (Albrecht et al. 2006) proposed a figure of merit (FoM) for cosmological measurements equal to the inverse of the area of the 95% confidence contour in the $w_0 - w_a$ plane. When we make this measurement, using the $\Delta\chi^2 = 5.99$ contour, we find a FoM of 1.84 (statistical-only) and 1.04 (including systematics). Frequently, the FoM is also defined in terms of the 1σ errors ($\Delta\chi^2 = 1$); this FoM is 39.3 (statistical-only) and 22.6 (including systematics). Surprisingly, even with w_a floating, we still find an interesting constraint on Ω_k of ~ 0.02.

We next consider a model in which the dark-energy equation-of-state parameter is constant inside fixed redshift bins. This model has more parameters (and thus more freedom) than $w_0 - w_a$. The results are shown in Figure 8 and Table 7. We adopt the redshift bins used in Amanullah et al. (2010), so that a direct comparison can be made.

In the left panel with broad bins, we show a reasonably good measurement of the equation-of-state parameter from redshift 0 to 0.5. From redshift 0.5 to 1, there is no real constraint. For example, any scalar field model ($|w| < 1$)

is reasonably compatible with the data. Above redshift 1, the constraints are weaker. $w \gtrsim 0$ is ruled out, as this violates early matter domination.

We separate the supernova and early universe constraints by defining a bin at redshift 1.6, as shown in the middle panel. This shifts the confidence interval for $w(1.0 < z < 1.6)$ towards higher w. Eliminating this division, and instead adding more bins up to redshift 0.5 (right panel), gives three constraints of moderate quality with a possible crossing of $w = -1$. No matter the binning, we will need more data extending above redshift 1 to investigate the dark energy equation-of-state parameter where the uncertainty is still very large.

To examine constraints on the existence of dark energy at different epochs, we study $\rho(z)$, which is the density of the dark energy and allowed to have different values in fixed redshift bins. Within each bin, ρ is constant. (Note that the discontinuities in $\rho(z)$ at the bin boundaries introduce discontinuities in $H(z)$.) We choose the same binning as above, but note that binned ρ and binned w models give different expansion histories. Our results are shown in Figure 9 and Table 8.

Although there is no real constraint on the equation-of-state parameter at redshift 0.5 to 1, dark energy is seen at high sig-
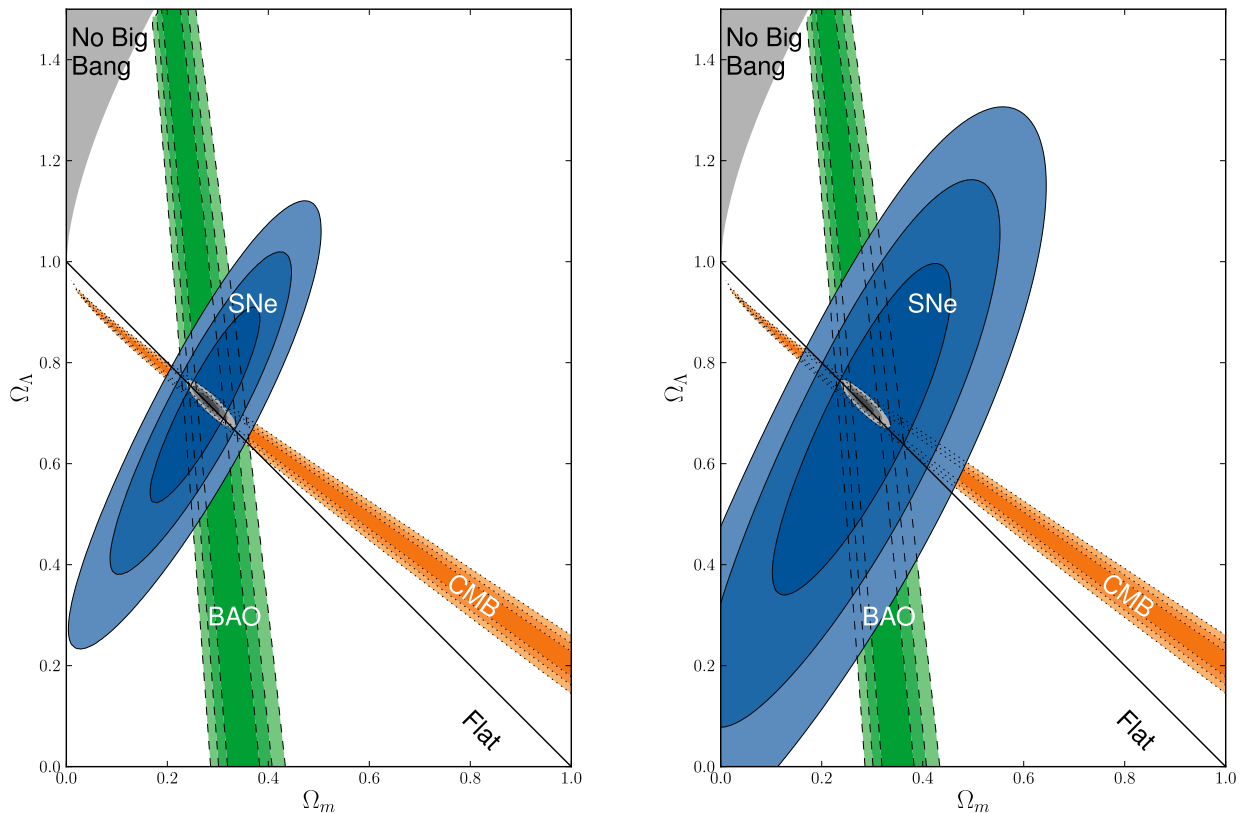
Figure 5. ΛCDM model: 68.3%, 95.4%, and 99.7% confidence regions of the $(\Omega_m, \Omega_\Lambda)$ plane from SNe Ia combined with the constraints from BAO and CMB. The left panel shows the SN Ia confidence region only including statistical errors while the right panel shows the SN Ia confidence region with both statistical and systematic errors.
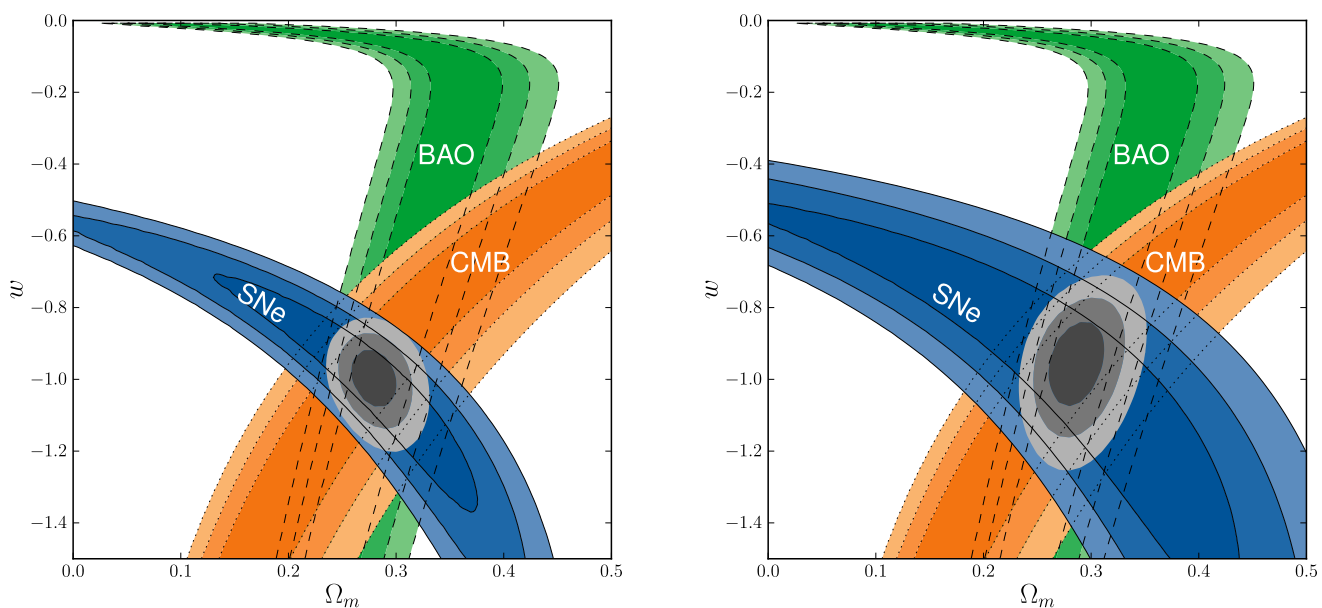

Figure 6. wCDM model: 68.3%, 95.4%, and 99.7% confidence regions in the (Ω_m, w) plane from SNe Ia BAO and CMB. The left panel shows the SN Ia confidence region for statistical uncertainties only, while the right panel shows the confidence region including both statistical and systematic uncertainties. We note that CMB and SN Ia constraints are orthogonal, making this combination of cosmological probes very powerful for investigating the nature of dark energy.

nificance in both panels. There is weak evidence for the existence of dark energy above redshift 1, as can be seen in the left panel. However, if we again separate the supernova data and early universe constraints (right panel) we see neither probe has any constraint on the existence of dark energy above redshift 1.

6. DISCUSSION

6.1. *Improving the Constraints on Time-Varying w by Efficiently Adding $z > 1$ Supernovae*

Beyond $z = 1$, we add 10 new well-measured SNe Ia to the Hubble diagram. The variance-weighted RMS scatter of the new sample is 0.20 ± 0.05 mag. As a comparison, the 15 $z > 1$ SNe Ia from the GOODS survey that pass our Union2 selection cuts have a variance-weighted RMS scatter of 0.25 ± 0.05 mag. The new sample almost doubles the weight of HST-discovered SNe Ia beyond $z = 1$. The increase provides improvements on the most difficult-to-measure parameters, those that describe the time-varying properties of dark energy: $\rho(z)$ and $w(z)$ at the higher redshifts. In particular, the supernovae from this search improve the constraint on $\rho(z)$ at redshifts $1.0z < 1.6$ by 28% (statistical errors only) and 18% (including supernova systematics) after adding the constraints from the CMB, BAO and H_0 (using the binning illustrated in the right panel of Figure 9). (It is more difficult to compare binned w results, as the constraints are much less gaussian and more sensitive to the location of the best fit.)

The new sample is also obtained with greater observing efficiency with HST. Considering the number of $z > 1$ SNe Ia that make the Union2 selection cuts, the yield of SNe Ia increases from a rate of one SN Ia per 43 HST orbits in the GOODS survey to one SN Ia per 22 HST orbits in this survey.

6.2. *Splitting the sample according to host galaxy type*

SNe Ia are well-standardized with a small dispersion in magnitudes across the whole class. Any clues to heterogeneous characteristics therefore offer exciting possibilities to *further* improve standardization, enhancing the use of SNe as a cosmological probe. There is now evidence from studies of large samples of SNe Ia at both low and intermediate redshifts ($0 < z \lesssim 0.8$) that SN Ia properties are related to the properties of the host. The clearest of these is the relation between light curve width and the specific star formation rate. SNe Ia in passive galaxies tend to have narrower light curves than SNe Ia that are in galaxies that are actively forming stars.

More than two-thirds of our new SNe Ia beyond $z = 0.9$ are hosted by early-type galaxies (Meyers et al. (2011)). In field surveys, such as the GOODS survey, this ratio is inverted. By combining SNe Ia from our HST Cluster SN Survey and GOODS, together with our $z > 0.9$ SNe Ia in Amanullah et al. (2010), which have HST images of the host, we can create a sample of SNe Ia that has roughly equal numbers when split according to host type. When split this way, we find that $z > 1$ SNe Ia in early galaxies rise and fall more quickly than SNe Ia in later host types, thus extending the redshift interval over which the effect is now detected. Finding that low and high redshift SNe Ia follow similar trends gives us confidence that we can use very distant events to constrain cosmological parameters. This finding is reported in more detail in Meyers et al. (2011).

There is also evidence from SNe Ia at low and intermediate redshifts for other correlations with host type. Sullivan et al. (2010) find that both β and the RMS scatter about the Hubble

diagram are smallest for SNe Ia in passive galaxies. These trends suggest that dust plays a greater role in reddening and dimming SNe Ia in late-type galaxies. We examined our $z > 0.9$ sample for evidence of similar correlations using our host classification from Tables 3 and 4 of Meyers et al (2011).

After correcting SN Ia luminosities for lightcurve shape, SN Ia color and host galaxy mass (with the global values of these correction coefficients), we measure a sample dispersion of $0.14^{+0.11}_{-0.08}$ mag for SNe Ia in early-type galaxies and $0.14^{+0.06}_{-0.05}$ mag for SNe Ia in late-type galaxies. In terms of the RMS, we find 0.23 ± 0.05 mag and 0.26 ± 0.05 mag for early and late-type samples, respectively. The uncertainties are currently too large to distinguish between the two samples. Similarly for β, the errors are larger than the difference between the two samples, as seen in Table 6. Clearly, higher quality data of a larger number of $z > 0.9$ SNe Ia in both early and late-type galaxies are required before the trends that are seen at low redshift can be detected in high redshift samples.

We also examined the error-weighted difference in the brightness of SNe Ia in the two samples after correcting for lightcurve shape and color, but without correcting for the host-mass luminosity relation (setting $\delta = 0$) and find that SNe Ia in early-type galaxies are 0.18 ± 0.09 mag brighter. Since early-type galaxies are typically more massive than late-type galaxies, this 2σ difference, if confirmed with larger statistics, may be related to host galaxy mass.

6.3. *Future directions with current instrumentation.*

Due to the much improved sensitivity of the WFC3 IR detector, it will be feasible to measure $z > 1$ SNe with much better precision. The color measurement errors (~ 0.03 in $B - V$) can be made comparable to the color measurement errors in the SDSS supernova survey (Smith et al. 2002; Holtzman et al. 2008). Assuming that the intrinsic dispersion of SN Ia luminosities does not change with redshift, the variance weighted RMS of the WFC3 sample should be similar to that measured for the SDSS, i.e. ~ 0.14 mag. A well-observed SN Ia with WFC3 should have a statistical weight of two to three SNe Ia from the Cluster and GOODS surveys.

With a sufficient number of well-measured $z > 1$ SNe Ia with WFC3, it should be possible to search for the correlations between the properties of SNe Ia and their hosts that are seen at lower redshifts. As discussed above, current samples at $z > 1$ are too small to detect these differences. With the improved WFC3 photometry, only 40 SNe Ia, split evenly between early and late-type hosts, would be needed to constrain a difference in β to an uncertainty of 0.4, which is about half the difference found for lower redshift SNe Ia (Sullivan et al. 2010). These samples would be just enough to see evidence of the lower RMS for passive hosts seen by Sullivan et al. (2010).

Current WFC3 SN Ia surveys target empty fields, which means that there will be few SNe Ia in passive host galaxies. A WFC3 SN Ia survey that spends part of its time targeting $z \gtrsim 1$ clusters would ensure a better balance between host types while increasing the overall yield.

In order to investigate the figure of merit constraints possible with WFC3, we simulate a sample of 40 supernovae at redshift 1.2 and add this sample into the current compilation. As there is a hard wall at $w_0 + w_a = 0$ when including BAO and CMB data, we simply fix Ω_m, rather than including BAO and CMB data (the alternative would be to adjust the supernova magnitudes to a cosmology model far away from the wall). When adding these supernovae, the statistical figure

Table 8

Constraints on redshift binned equation of state w and density ρ (normalized by the current critical density). The constraints are computed including SNe, BAO, H_0, and CMB data.

		z < 0.5	0.5 < z < 1.0	1.0 < z < 1.6	z > 1.6 [a]
$w(z)$	Stat Only:	$-1.013^{+0.067}_{-0.069}$	$-0.78^{+0.58}_{-0.68}$	$-3.7^{+2.2}_{-4.4}$	< 0.18
	w/ Sys:	$-1.006^{+0.110}_{-0.113}$	$-0.69^{+0.80}_{-0.98}$	$-3.9^{+3.2}_{-8.2}$	< 0.24
$\rho_{\rm DE}(z)/\rho_{c0}$	Stat Only:	$0.732^{+0.013}_{-0.014}$	$0.85^{+0.18}_{-0.17}$	$0.23^{+1.29}_{-0.79}$	$0.9^{+1.9}_{-1.5}$
	w/ Sys:	$0.731^{+0.014}_{-0.015}$	$0.88^{+0.24}_{-0.21}$	$0.33^{+1.90}_{-1.00}$	$0.7^{+2.4}_{-1.8}$

Note. — Constraints on binned $\rho_{\rm DE}(z)/\rho_{c0}$ and $w(z)$. This redshift binning corresponds to the middle panel of Figure 8 and the right panel of Figure 9

[a] We note that the weak constraints in these bins come mostly from the CMB (which tells us that the early universe was matter-dominated) and are only indirectly constrained by supernovae.

of merit improves by 39%. By the same metric, the current cluster sample improves the figure of merit by 10%.

6.4. *Reducing the Systematic Errors for Future Surveys*

As has been stressed by several authors, systematic errors are now larger than statistical errors. To fully utilize the potential of current and future SN Ia surveys to constrain cosmology, it will be necessary to reduce these errors significantly.

The largest current source of systematic uncertainty is calibration. Calibration uncertainties can be split into uncertainties related to the primary standard, and uncertainties in instrumental zeropoints and band passes. In principle, all of these uncertainties can be reduced by establishing a network of well-calibrated standard stars and monitoring telescope system throughputs (Regnault et al. 2009). The Sloan Digital Sky Survey demonstrated that a 1% relative photometric calibration is possible with the current standard star network and system throughput monitoring (Doi et al. 2010).

The ongoing Nearby Supernova Factory (SNf) project (Aldering et al. 2002) is aiming to provide the network of standard stars. SNf will also address the systematic uncertainty due to host-mass correction since the range of host masses would become comparable to that of high redshift for the first time. Additionally, the comprehensive SN Ia spectral time series from the SNf will allow one to tackle systematic uncertainties related to modeling of the lightcurves.

In the future, recently approved experiments such as ACCESS (Absolute Color Calibration Experiment for Standard Stars Kaiser et al. 2010) and the proposed NIST STARS project (National Institute for Standards and Technology McGraw et al. 2010; Zimmer et al. 2010) are aiming to achieve sub-percent absolute flux calibration for the network of stars in the wavelength range of visible to NIR. With this network of stars and with new techniques for monitoring throughput of the telescopes (Stubbs et al. 2007), we will be able to cross-calibrate systems and reduce the systematic errors below the statistical errors.

7. SUMMARY AND CONCLUSIONS

We present HST ACS, HST NICMOS and Keck AO-assisted photometry of 20 SNe Ia in the redshift range $0.63 < z < 1.42$. The SNe Ia were discovered in the HST Cluster Supernova Survey, a survey run by the Supernova Cosmology Project to search for SNe Ia in fields centered on 25 distant galaxy clusters (Dawson et al. 2009).

We implement new techniques to improve the accuracy of HST photometry. In particular, for data taken with NICMOS, which samples the rest-frame B and V-bands of $z > 1$

SNe Ia, we use a more direct, more accurate measure of the NICMOS zeropoint (Ripoche et al. 2011), and we remove the residual background that persists after standard processing of NICMOS data with the CALNICA pipeline (Hsiao et al. 2010). For data taken with ACS WFC in the z_{850} filter, we incorporate a SED-dependent aperture correction (see Appendix A).

Following the procedures outlined in Kowalski et al. (2008) and Amanullah et al. (2010), we add our SNe Ia to the Union2 compilation. Fourteen of the 20 SNe Ia of our supernovae pass the Union2 selection cuts. Ten of them are at $z > 1$. The strategy of targeting high-redshift galaxy clusters results in factor of two improvement in the yield per HST orbit of well-measured SNe Ia beyond $z = 1$ and a factor of three to five improvement for SNe hosted by early-type galaxies. For WFC3, with its smaller field of view, the advantage of a cluster search is even greater.

We use the new Union2.1 sample to constrain the properties of dark energy. SNe Ia alone constrains the existence of dark energy to very high significance. After adding constraints from the CMB, BAO, and H_0 measurements, we provide the tightest limits yet on the evolution of dark energy with time: $w_a = 0.14^{+0.60}_{-0.76}$. Our sample improves the constraints on binned ρ by 18% in the difficult-to-measure high redshift bin, $1.0 < z < 1.6$. Even with a time-varying w_0-w_a model, the universe is constrained to be flat with an accuracy of 2% in Ω_k.

The results from this new cluster-hosted supernova sample point the way to the next steps that are now possible with the WFC3 on HST, an instrument that can obtain high signal-to-noise, multifilter SN Ia lightcurves at $z > 1$. The cluster approach, used in this paper, would make it feasible to build a significantly larger sample at these highest redshifts, evenly balanced between early and late-type hosts. With such a sample, we can mitigate the effects of dust and evolution that may ultimately limit constraints on time-varying w.
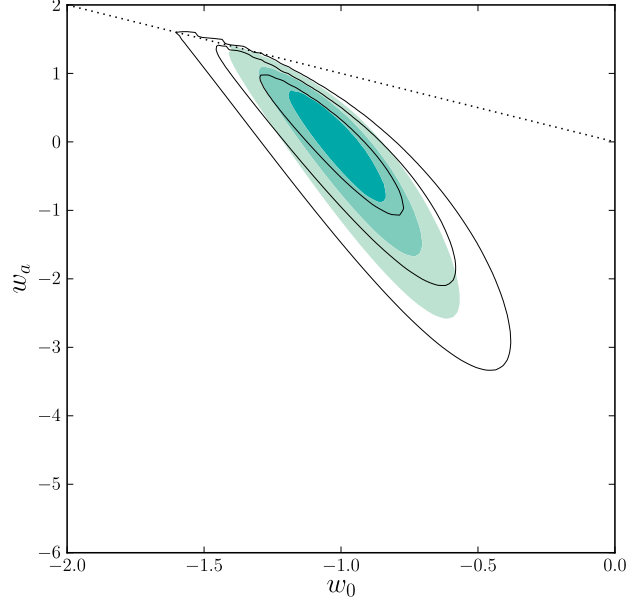
Figure 7. 68.3%, 95.4%, and 99.7% confidence regions of the (w_0, w_a) plane from SNe combined with the constraints from BAO, CMB, and H_0, both with (solid contours) and without (shaded contours) systematic errors. Zero curvature has been assumed. Points above the dotted line ($w_0 + w_a > 0$) violate early matter domination and are disfavored by the data.
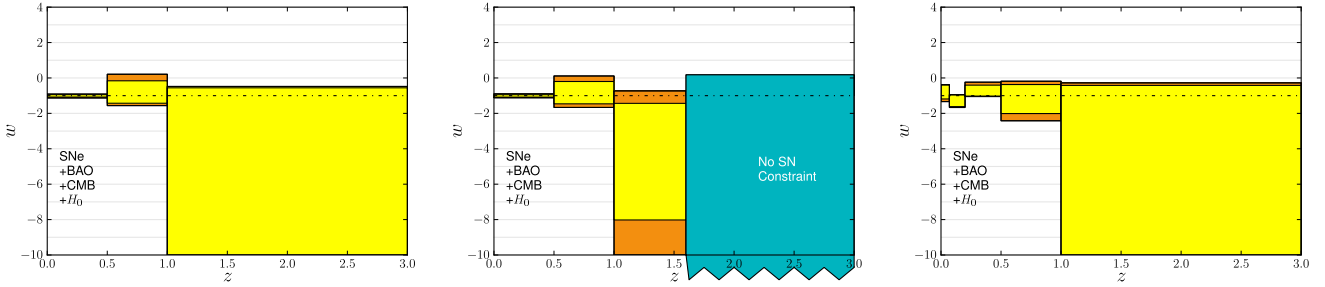

Figure 8. Constraints on $w(z)$, where $w(z)$ is assumed to be constant in each redshift bin, are plotted at the 68% probability level ($\Delta\chi^2 = 1$). Each panel shows different redshift binning. The results were obtained assuming a flat universe for the joint data set of SNe, BAO, CMB, and H_0, with (dark/orange) and without (light/yellow) SN systematics. The middle panel takes a closer look at the $z > 1$ constraints, while the right panel shows the effects of w binning at low redshift. In this panel the best fit values of w cross $w = -1$ twice at low redshift, an unusual feature in dark energy models. We note that the ΛCDM model is consistent with our $w(z)$ constraints for each of these binnings.
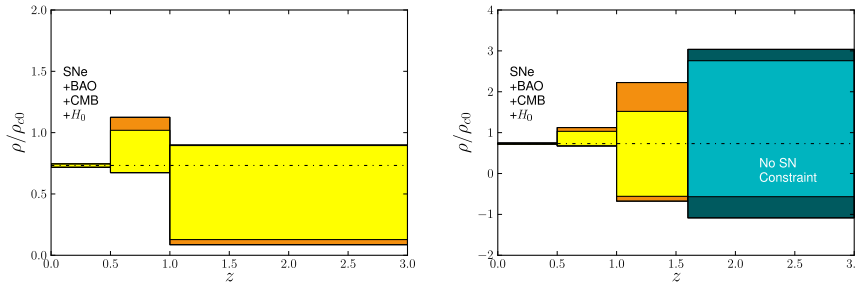
Figure 9. Redshift evolution of dark energy density: Constraints on $\rho(z)$ are shown as a function of redshift, where $\rho(z)$ is the density of the dark energy at a given redshift bin and assumed to be constant within the redshift bin. $\rho(z)$ is normalized by the critical density today (ρ_{c0}) and is plotted at the 68% probability level ($\Delta\chi^2 = 1$). The results were obtained assuming a flat Universe for the joint data set of SNe Ia, BAO, CMB, and H_0, with (dark/orange) and without (light/yellow) SN systematics. The two panels demonstrate different redshifts binning and have different scales.

APPENDIX

APPENDIX : ACS COLOR DEPENDENT APERTURE CORRECTION

The scattering of long wavelength photons (> 8000 Å) within the ACS CCDs causes the point spread function (PSF) of images taken in the ACS z_{850}-band to depend on the spectral energy distribution (SED) of the source (Sirianni et al. 2005; Jee et al. 2007). The SED-dependent PSF means that aperture corrections also depend on the SED. In this section, we describe how we derive aperture corrections for our observations taken with the ACS z_{850}-band.

We use two stars (GRW70 and GD72 from ACS programs PID9020 and PID10720) to measure the aperture correction (AC) as a function of wavelength. The stars were observed with 15 narrow-band filters between 7660Å and 10360Å. We processed the data in the same way as the SN Ia images. To derive the aperture correction, we compare the flux in two apertures, one with a 3-pixel radius and the other with a 110-pixel radius (the radius used for defining the zeropoint). Errors from removing the sky are the dominant source of the uncertainty of this measurement.

The measured encircled energy and its best-fit curve for a 3-pixel radius are shown as a function of wavelength in Figure 10. We apply an aperture correction to the observed flux with this best-fit curve. Figure 11 demonstrates that the i_{775}- z_{850} color is not accurate enough for SNe Ia to infer the accurate aperture correction. Therefore, we need to introduce an SED-weighted aperture correction.
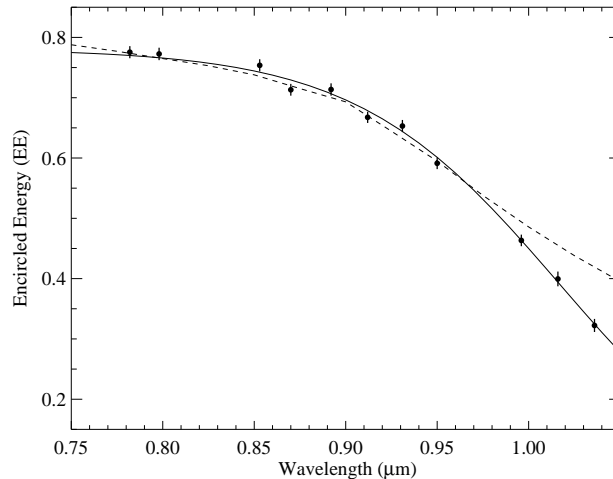

Figure 10. Wavelength vs. Encircled Energy (EE) Fraction for a 3-pixel aperture. The solid line is a fit (Eq. A1) to the measured data points. The dotted line is the relation from Sirianni et al. (2005).

We find that the best-fit encircled energy curve can be described with

$$\mathrm{EE}(\lambda) = \frac{1}{1.28 + 1.45 \times 10^{-8} \times \exp(17.99 \times \lambda)} \tag{A1}$$

where λ is wavelength in μm. The formula is valid in wavelength for virtually all the F850LP filter.

Since the SED of a SN Ia is a function of redshift and phase, so is the aperture correction. We demonstrate two methods to account for this dependence. The first method, "Method I," calculates the aperture correction iteratively using the SED produced by SALT2. The advantage of this method is that the final aperture-corrected fluxes can be used with the standard throughputs and zeropoints. The second method, "Method II," computes a new zeropoint and F850LP throughput for direct use with the flux measurements that have not been aperture-corrected. We note here that an apparent color difference between SNe with only ACS data and those that also had NICMOS observations was seen unblinded *before* the development of these methods, so the relative colors of the ACS-only and NICMOS-included subsamples should not be considered blinded.
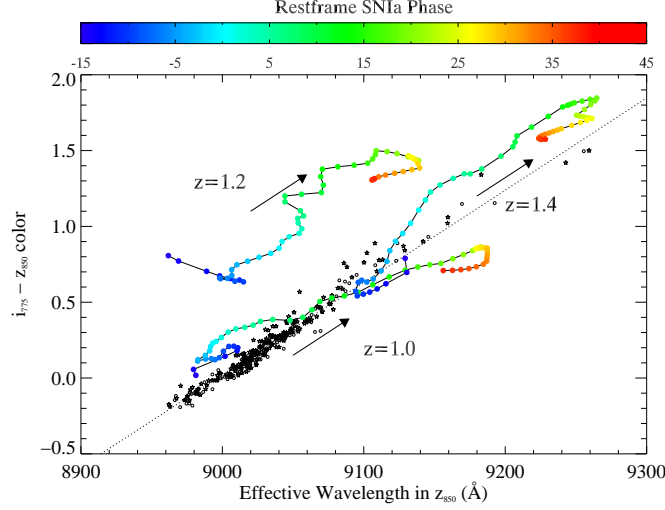
Figure 11. Wavelength vs. $i_{775} - z_{850}$ color: solid asterisks are stars from Gunn-Stryker Catalog (Gunn & Stryker 1983); open asterisks are stars from Pickles catalog (Pickles 1998). The dotted line is the best-fit line to the stellar locus. SN Ia loci (Hsiao et al. 2007) are plot for three redshifts with color-coded phases and arrows which show the direction of the phase evolution. The SN Ia loci deviate from the stellar locus as the SED is different. Therefore, $i_{775} - z_{850}$ colors are not accurate enough to perform aperture corrections, necessitating the introduction of an SED-weighted aperture correction.

Both methods give the same answer, although the error in the color from "Method II" is slightly larger than that of "Method I", because the effective wavelength of the z_{850} shifts towards the i_{775} filter, thus shortening the wavelength separation of the two filters. For this paper, we adopt "Method II" and report all results using this method.

Method I: Iterative approach

The magnitude of an object in the Vega magnitude system is defined (Fukugita et al. 1995; Sirianni et al. 2005) as

$$m = -2.5 log_{10}\left(\frac{\int \lambda R f_\lambda d\lambda}{\int \lambda R f_{\lambda \mathrm{Vega}} d\lambda}\right), \tag{A2}$$

where λ is wavelength, R is the system response, f_λ is the SED of the object (e.g. SN Ia), and $f_{\lambda \mathrm{Vega}}$ is the SED of Vega. We define the Vega magnitude zeropoint (Zpt) as

$$\mathrm{Zpt_{Vega}} = 2.5 log_{10}\left(\int \lambda R f_{\lambda \mathrm{Vega}} d\lambda\right). \tag{A3}$$

Eq. A2 can then be rewritten as:

$$m = -2.5 log_{10}\left(\int \lambda R f_\lambda d\lambda\right) + \mathrm{Zpt_{Vega}}. \tag{A4}$$

The observed magnitude, m_{obs}, within a given aperture is

$$m_{\mathrm{obs}} = -2.5 log_{10}\left(\int \lambda R \, \mathrm{EE}(\lambda) \, f_\lambda d\lambda\right) + \mathrm{Zpt_{Vega}}, \tag{A5}$$

where $\mathrm{EE}(\lambda)$ is the wavelength dependent encircled energy (EE), which can be derived from Eq. A1.

We define the SED dependent aperture correction (Δm_{corr}) as

$$\Delta m_{\mathrm{corr}} = -2.5 log_{10}\left(\frac{\int \lambda R \, \mathrm{EE}(\lambda) \, f_\lambda d\lambda}{\int \lambda R f_\lambda d\lambda}\right) \tag{A6}$$

In practice, we do not know f_λ in advance, so we cannot compute the aperture correction directly. Instead, we derive it iteratively using the SED derived from fitting the SN Ia light curve with SALT2 as input to the next iteration. With this method, we use the STScI filter response function and zeropoints.

Method II: Modified Filter with Zeropoint

We can rewrite Eq. A5 as:

$$m_{\mathrm{obs}} = -2.5 log_{10}\left(\frac{\int \lambda R \, \mathrm{EE}(\lambda) f_\lambda d\lambda}{\int \lambda R \, \mathrm{EE}(\lambda) f_{\lambda \mathrm{Vega}} d\lambda}\right) + \mathrm{Zpt_{Vega}} - 2.5 log_{10}\left(\int \lambda R \, \mathrm{EE}(\lambda) \, f_{\lambda \mathrm{Vega}} d\lambda\right). \tag{A7}$$

Effectively, the last term serves as a zeropoint offset for a given aperture radius.
We rewrite Eq. A7 as:

$$m_{\rm obs} = -2.5log_{10}\left(\frac{\int \lambda\,R\,{\rm EE}(\lambda)\,f_\lambda d\lambda}{\int \lambda\,R\,{\rm EE}(\lambda)\,f_{\lambda{\rm Vega}}d\lambda}\right) + {\rm Zpt}_{\rm Vega} - \Delta{\rm Zpt}_{\rm Vega}, \qquad (A8)$$

$\Delta{\rm Zpt}_{\rm Vega} = 0.438$ for a 3-pixel radius aperture and the z_{850} filter. We interpret Eq. A8 as a magnitude measurement that uses a modified filter response, $R\,{\rm EE}(\lambda)$, and an adjusted zeropoint, ${\rm Zpt}_{\rm Vega} - \Delta{\rm Zpt}_{\rm Vega}$. We then run SALT2 using the counts in a fixed aperture, the modified filter response and the adjusted zeropoint.

<div align="center">REFERENCES</div>

Albrecht, A., et al. 2006, astro-ph/0609591
Aldering, G., et al. 2002, in Presented at the Society of Photo-Optical Instrumentation Engineers (SPIE) Conference, Vol. 4836, Survey and Other Telescope Technologies and Discoveries. Edited by Tyson, J. Anthony; Wolff, Sidney. Proceedings of the SPIE, Volume 4836, pp. 61-72 (2002)., ed. J. A. Tyson & S. Wolff, 61–72
Amanullah, R., et al. 2010, ApJ, 716, 712
Amanullah, R., et al. 2008, A&A, 486, 375
Anderson, J. 2007, Variation of the Distortion Solution, Tech. rep.
Astier, P., et al. 2006, A&A, 447, 31
Barbary, K., et al. 2010, arXiv:1010.5786
Barbary, K., et al. 2009, ApJ, 690, 1358
Barker, E. A., Laidler, V. G., & Koekemoer, A. M. 2007, Removing Post-SAA Persistence in NICMOS Data, Tech. rep.
Beckwith, S. V. W., et al. 2006, AJ, 132, 1729
Blakeslee, J. P., et al. 2003, ApJ, 596, L143
Bohlin, R. C. 2007, Photometric Calibration of the ACS CCS Cameras, Tech. rep.
Bohlin, R. C., J., L. D., & Riess, A. 2005, Grism Sensitivities and Apparent Non-Linearity, Tech. rep.
Bohlin, R. C., Riess, A., & de Jong, R. 2006, NICMOS Count Rate DependentNon-Linearity in G096 and G141, Tech. rep.
Bohringer, H., Mullis, C., Rosati, P., Lamer, G., Fassbender, R., Schwope, A., & Schuecker, P. 2005, The Messenger, 120, 33
Bouwens, R. J., Illingworth, G. D., Blakeslee, J. P., & Franx, M. 2006, ApJ, 653, 53
Brodwin, M., et al. 2010, arXiv:1012.0581
Bruzual, G. & Charlot, S. 2003, MNRAS, 344, 1000
Bundy, K., Ellis, R. S., & Conselice, C. J. 2005, ApJ, 625, 621
Conley, A., et al. 2006, AJ, 132, 1707
Contreras, C., et al. 2010, AJ, 139, 519
Copeland, E. J., Sami, M., & Tsujikawa, S. 2006, International Journal of Modern Physics D, 15, 1753
Dahlen, T., McLaughlin, H., Laidler, V., Regan, M., Bergeron, R., E., J., Bohlin, R., & de Jong, R. a. 2008, Improvements to Calnica, Tech. rep.
Dawson, K. S., et al. 2009, AJ, 138, 1271
de Jong, R. S., Bergeron, E., Riess, A., & Bohlin, R. 2006, NICMOS count-rate dependent nonlinearity tests using flatfield lamps, Tech. rep.
Dickinson, M., Giavalisco, M., & GOODS Team. 2003, in The Mass of Galaxies at Low and High Redshift, ed. R. Bender & A. Renzini, 324–+
Doi, M., et al. 2010, AJ, 139, 1628
Duffy, A. R., Schaye, J., Kay, S. T., & Dalla Vecchia, C. 2008, MNRAS, 390, L64
Dunkley, J., et al. 2009, ApJS, 180, 306
Eisenhardt, P. R. M., et al. 2008, ApJ, 684, 905
Eisenstein, D. J., et al. 2005, ApJ, 633, 560
Fruchter, A. S. & Hook, R. N. 2002, PASP, 114, 144
Fukugita, M., Ichikawa, T., Gunn, J. E., Doi, M., Shimasaku, K., & Schneider, D. P. 1996, AJ, 111, 1748
Fukugita, M., Shimasaku, K., & Ichikawa, T. 1995, PASP, 107, 945
Garnavich, P. M., et al. 1998, ApJ, 509, 74
Gilbank, D. G., Gladders, M. D., Yee, H. K. C., & Hsieh, B. C. 2010, arXiv:1012.3470
Gladders, M. D. & Yee, H. K. C. 2005, ApJS, 157, 1
Gunn, J. E. & Stryker, L. L. 1983, ApJS, 52, 121
Guth, A. H. 1981, Phys. Rev. D, 23, 347
Guy, J., et al. 2007, A&A, 466, 11
Guy, J., Astier, P., Nobili, S., Regnault, N., & Pain, R. 2005, A&A, 443, 781
Guy, J., et al. 2010, arXiv:1010.4743
Hamuy, M., Phillips, M. M., Suntzeff, N. B., Schommer, R. A., Maza, J., & Aviles, R. 1996, AJ, 112, 2391
Hamuy, M., Trager, S. C., Pinto, P. A., Phillips, M. M., Schommer, R. A., Ivanov, V., & Suntzeff, N. B. 2000, AJ, 120, 1479
Heyer, I., Richardson, M., Whitmore, B., & Lubin, L. 2004, The Accuracy of WFPC2 Photometric Zeropoints, Tech. rep.
Hicken, M., et al. 2009a, ApJ, 700, 331
Hicken, M., Wood-Vasey, W. M., Blondin, S., Challis, P., Jha, S., Kelly, P. L., Rest, A., & Kirshner, R. P. 2009b, ApJ, 700, 1097
—. 2009c, ApJ, 700, 1097
Hilton, M., et al. 2007, ApJ, 670, 1000
Hilton, M., et al. 2009, ApJ, 697, 436
Holtzman, J. A., et al. 2008, AJ, 136, 2306
Hsiao, E. Y., Conley, A., Howell, D. A., Sullivan, M., Pritchet, C. J., Carlberg, R. G., Nugent, P. E., & Phillips, M. M. 2007, ApJ, 663, 1187
Hsiao, E. Y., et al. 2011, in The 2010 HST Calibration Workshop, ed. S. Deustua, C. Oliveira
Huang, X., et al. 2009, ApJ, 707, L12
Jee, M. J., Blakeslee, J. P., Sirianni, M., Martel, A. R., White, R. L., & Ford, H. C. 2007, PASP, 119, 1403
Jee, M. J., et al. 2011, arXiv:1105.3186
Jee, M. J., et al. 2009, ApJ, 704, 672
Kaiser, M. E., et al. 2010, ArXiv e-prints
Kelly, P. L., Hicken, M., Burke, D. L., Mandel, K. S., & Kirshner, R. P. 2010, ApJ, 715, 743
Kessler, R., et al. 2009, ApJS, 185, 32
Knop, R. A., et al. 2003, ApJ, 598, 102
Koekemoer, A. M., Fruchter, A. S., Hook, R. N., & Hack, W. 2002, in The 2002 HST Calibration Workshop : Hubble after the Installation of the ACS and the NICMOS Cooling System, ed. S. Arribas, A. Koekemoer, & B. Whitmore, 337
Komatsu, E., et al. 2011, ApJS, 192, 18
Kowalski, M., et al. 2008, ApJ, 686, 749
Kuznetsova, N., et al. 2008, ApJ, 673, 981
Lampeitl, H., et al. 2010, ApJ, 722, 566
Liddle, A. R. & Lyth, D. H. 2000, Cosmological Inflation and Large-Scale Structure, ed. Liddle, A. R. & Lyth, D. H.
Linder, E. V. 2003, Physical Review Letters, 90, 091301

Mannucci, F., Della Valle, M., Panagia, N., Cappellaro, E., Cresci, G., Maiolino, R., Petrosian, A., & Turatto, M. 2005, A&A, 433, 807
Maraston, C. 2005, MNRAS, 362, 799
McGraw, J. T., et al. 2010, in Society of Photo-Optical Instrumentation Engineers (SPIE) Conference Series, Vol. 7739, Society of Photo-Optical Instrumentation Engineers (SPIE) Conference Series
Mei, S., et al. 2006, ApJ, 639, 81
Melbourne, J., et al. 2007, AJ, 133, 2709
Melbourne, J., et al. 2005, ApJ, 625, L27
Ménard, B., Kilbinger, M., & Scranton, R. 2010, MNRAS, 406, 1815
Meyers, J., et al. 2011, ApJ *submitted*
Mobasher, B. & Riess, A. 2005, A Test of Possible NICMOS Non-linearity, Tech. rep.
Morokuma, T., et al. 2010, PASJ, 62, 19
Navarro, J. F., Frenk, C. S., & White, S. D. M. 1997, ApJ, 490, 493
Norgaard-Nielsen, H. U., Hansen, L., Jorgensen, H. E., Aragon Salamanca, A., & Ellis, R. S. 1989, Nature, 339, 523
Peng, C. Y., Ho, L. C., Impey, C. D., & Rix, H. 2002, AJ, 124, 266
Percival, W. J., et al. 2010, MNRAS, 401, 2148
Perlmutter, S., et al. 1998, Nature, 391, 51
Perlmutter, S., et al. 1999, ApJ, 517, 565
Perlmutter, S., Marvin, H. J., Muller, R. A., Pennypacker, C. R., Sasseen, T. P., Smith, C. K., & Wang, L. P. 1991, in Supernovae, ed. S. E. Woosley, 727–+
Pickles, A. J. 1998, PASP, 110, 863
Postman, M., et al. 2005, ApJ, 623, 721
Postman, M., Lubin, L. M., Gunn, J. E., Oke, J. B., Hoessel, J. G., Schneider, D. P., & Christensen, J. A. 1996, AJ, 111, 615
Regnault, N., et al. 2009, A&A, 506, 999
Riess, A. & Bergeron, E. 2008, Bright Earth Persistence in NICMOS, Tech. rep.
Riess, A. & Mack, J. 2004, Time Dependence of ACS WFC CTE Corrections for Photometry and Future Predictions, Tech. rep.
Riess, A. G., et al. 1998, AJ, 116, 1009
Riess, A. G., et al. 1999, AJ, 117, 707
Riess, A. G., et al. 2011, ApJ, 730, 119
Riess, A. G., et al. 2004, ApJ, 607, 665
Riess, A. G., et al. 2007, ApJ, 659, 98
Ripoche, P., et al. 2011, ApJ *submitted*
Rosati, P., Stanford, S. A., Eisenhardt, P. R., Elston, R., Spinrad, H., Stern, D., & Dey, A. 1999, AJ, 118, 76
Rosati, P., et al. 2009, A&A, 508, 583
Sahlén, M., et al. 2009, MNRAS, 397, 577
Sand, D. J., et al. 2010, arXiv:1011.1310
Santos, J. S., et al. 2009, A&A, 501, 49
Schlegel, D. J., Finkbeiner, D. P., & Davis, M. 1998, ApJ, 500, 525
Schmidt, B. P., et al. 1998, ApJ, 507, 46
Sirianni, M., et al. 1998, in Presented at the Society of Photo-Optical Instrumentation Engineers (SPIE) Conference, Vol. 3355, Society of Photo-Optical Instrumentation Engineers (SPIE) Conference Series, ed. S. D'Odorico, 608
Sirianni, M., et al. 2005, PASP, 117, 1049
Smith, J. A., et al. 2002, AJ, 123, 2121
Spergel, D. N., et al. 2003, ApJS, 148, 175
Strazzullo, V., et al. 2010, A&A, 524, 17
Stubbs, C. W., et al. 2007, PASP, 119, 1163
Sullivan, M., et al. 2010, MNRAS, 406, 782
Sullivan, M., et al. 2003, MNRAS, 340, 1057
Sullivan, M., et al. 2006, ApJ, 648, 868
Tremonti, C. A., et al. 2004, ApJ, 613, 898
Wood-Vasey, W. M., et al. 2007, ApJ, 666, 694
Zimmer, P. C., et al. 2010, in Society of Photo-Optical Instrumentation Engineers (SPIE) Conference Series, Vol. 7735, Society of Photo-Optical Instrumentation Engineers (SPIE) Conference Series